An optogenetic method for interrogating YAP1 and TAZ nuclear-cytoplasmic shuttling

Anna M. Dowbaj[1*], Robert P. Jenkins[1*], John M. Heddleston[2], Alessandro Ciccarelli[3], Todd Fallesen[3], Klaus Hahn[4], Marco Montagner[5¥], Erik Sahai[1¥]

1 Tumour Cell Biology Laboratory, The Francis Crick Institute, London, UK
2 Advanced Imaging Center, Janelia Research Campus, HHMI, Ashburn, VA, USA
3 Advanced Light Microscopy, The Francis Crick Institute, London, UK
4 University of North Carolina, Chapel Hill, NC, USA
5 Department of Molecular Medicine, University of Padova, Viale G. Colombo 3, 35126 - Padova, Italy

* these authors contributed equally

¥ authors for correspondence marco.montagner@unipd.it and erik.sahai@crick.ac.uk

Abstract

The shuttling of transcription factors and transcriptional regulators in and out of the nucleus is central to the regulation of many biological processes. Here we describe a new method for studying the rates of nuclear entry and exit of transcriptional regulators. A photo-responsive AsLOV (*Avena sativa* Light Oxygen Voltage) domain is used to sequester fluorescently-labelled transcriptional regulators YAP1 and TAZ/WWTR1 on the surface of mitochondria and reversibly release them upon blue light illumination. After dissociation, fluorescent signals from mitochondria, cytoplasm and nucleus are extracted with a bespoke app and used to generate rates of nuclear entry and exit. Using this method, we demonstrate that phosphorylation of YAP1 on canonical sites enhances its rate of nuclear export. Moreover, we provide evidences that, despite high intercellular variability, YAP1 import and export rates correlated within the same cell. By simultaneously releasing YAP1 and TAZ from sequestration, we show that their rates of entry and exit are correlated. Furthermore, tracking of light-sensitive YAP1 with lattice lightsheet microscopy revealed high heterogeneity of YAP1 dynamics within different subcellular regions, suggesting that implementing high resolution volumetric 3D data could shed light on new mechanisms of nuclear-cytoplasmic shuttling of proteins.

Introduction

Rapid regulation of cellular processes in space and time is mostly achieved either by switching on inactive proteins in the correct location, or by recruiting proteins at the appropriate subcellular compartment at the right time. Compartmentalisation is a fundamental feature of eukaryotic cells and numerous membrane bound organelles contribute to sub-cellular organisation. Shuttling of proteins between compartments is a key mechanism of regulating many processes, including the transcription of DNA in the nucleus (Fu et al., 2018, Xu and Massague, 2004, Di Ventura and Kuhlman, 2016). Transcription factors and transcriptional regulators are examples of proteins regulated by compartmentalisation and their nuclear accumulation is often restricted in absence of activating signals, either by cytoplasmic tethering or constitutive nuclear export (Xu and Massague, 2004). Mechanistically, members of the karyopherin family recognize specific signals on cargo proteins (larger than 40KDa), namely nuclear localization signals (NLS) and nuclear export signals (NES), and mediate their transition across the nuclear pore complex (NPC), while loading and unloading of cargoes are controlled by the GTPase Ran (Fu et al., 2018, Di Ventura and Kuhlman, 2016), thus representing an energetic barrier to NC shuttling. Importantly, the function of many transcription factors and regulators is the integration of several signaling inputs. The specificity of the response is dictated by the modulation of frequency, intensity and duration of nuclear-cytoplasmic (NC) shuttling rather than linear nuclear accumulation (Hao and O'Shea, 2011, Purvis and Lahav, 2013, Gao et al., 2018, Yosef and Regev, 2011, Behar and Hoffmann, 2010). This change in our understanding highlights the importance of live, non-destructive techniques.

YAP1 and TAZ transcriptional regulators are a perfect example of such complexity. They serve as a hub for a wide range of stimuli, including biochemical (Hippo, (Meng et al., 2016)) and metabolic pathways (Sorrentino et al., 2014, Bertolio et al., 2019), mechanical inputs (rigidity, shape, stiffness, cell density and shear stress) (Wada et al., 2011, Calvo et al., 2013, Benham-Pyle et al., 2015, Aragona et al., 2013, Dupont et al., 2011, Chaudhuri et al., 2016, Nakajima et al., 2017, Elosegui-Artola et al., 2017), polarity and other signalling cascades (GPCRs, Akt, JNK) (Calvo et al., 2013, Codelia et al., 2014, Basu et al., 2003) (Fig. S1A). YAP1 and TAZ are master regulators of cell proliferation, apoptosis, phenotypic plasticity (Zanconato et al., 2019, Shreberk-Shaked and Oren, 2019) and unsurprisingly they are involved in all the steps of tumorigenesis (Zanconato et al., 2016) (Fig. S1A). In the canonical view of the pathway, YAP1 and TAZ activity is inhibited by nuclear exclusion upon LATS1/2 (the main kinases of Hippo pathway downstream

of MST1/2) phosphorylation on key serine residues, and subsequent binding to 14-3-3 proteins or proteasomal degradation. When the phosphorylation is low, YAP1 and TAZ can accumulate into the nucleus and bind to their DNA-binding partners TEAD1-4, BRD4 and MED1, which also contribute to their nuclear accumulation. However, this over simplistic model has been challenged by recent findings that LATS-phosphorylated-YAP1 can be found in the nucleus and that nuclear accumulation is not sufficient for YAP1-driven transcriptional activity (Ege et al., 2018, Wada et al., 2011). Moreover, several LATS-independent mechanisms have been shown to affect YAP1 and TAZ NC shuttling and activity, such as nuclear deformation (Elosegui-Artola et al., 2017), cell cycle (Manning et al., 2018), Src family kinases (Calvo et al., 2013, Ege et al., 2018, Elbediwy et al., 2016, Rosenbluh et al., 2012, Tamm et al., 2011) and, more recently, phase separation (Lu et al., 2020, Cai et al., 2019). Despite the intense studies on these transcription regulators during the years, there is no consensus on how their NC shuttling is regulated.

Historically NC shuttling has been investigated with static methods, on fixed cells or subcellular fractions, with low temporal and spatial resolution, and using chemical such as the export inhibitor Leptomycin B. More recently, measurement of protein shuttling has been revolutionised by the use of fluorescent dyes and proteins (Molenaar and Weeks, 2018, Di Ventura and Kuhlman, 2016). Without perturbation, the partitioning of fluorescent signal between compartment reflects the equilibrium position of the various shuttling process influencing the fluorescently tagged protein. The application of light-driven perturbations, such as photobleaching, provides more information about rates of transit between compartments. However, one downside of photobleaching is that it is inherently destructive by irreversibly damaging the fluorophore, which limits the researcher's ability to make repeated measurements and typically generates only a single intensity decay curve, which limits the mathematical fitting to derive shuttling rates.

During the last decade, several optogenetic systems have been developed to control NC localisation of proteins within a few seconds upon light illumination. Early examples of light-mediated NC shuttling (Engelke et al., 2014, Crefcoeur et al., 2013) led to irreversible nuclear accumulation and they have been surpassed by reversible methods based on light-sensitive proteins. The common idea underlying optogenetic systems is the light-dependent conformational change of photoreceptors fused with the proteins of interest, that can be exploited to manipulate a wide range of cellular processes (de Mena et al., 2018). Desired protein localization upon light illumination has been achieved with two strategies so far: two-components systems, in which a bait protein is anchored to one compartment and the interaction with the prey protein is light-

84 dependent (Guntas et al., 2015, Kennedy et al., 2010, Beyer et al., 2015, Strickland et al., 2012),
85 and one-component systems, in which NES/NLS peptides are caged/exposed upon light
86 illumination (Niopek et al., 2014, Niopek et al., 2016, Yumerefendi et al., 2015, Yumerefendi et
87 al., 2016). Interestingly, the former strategy has been recently used to develop light-induced
88 control of cellular forces and, as a consequence, of YAP1 localisation (Valon et al., 2017). In this
89 work, we exploited an optogenetic tool, namely LOV-TRAP (Wang and Hahn, 2016, Wang et al.,
90 2016a), for studying NC shuttling based upon light-induced release and sequestration of the
91 protein of interest (POI). We present detailed methods for the molecular biology, imaging, and
92 analysis of this tool. Furthermore, the utility of the method is demonstrated by measuring the
93 nuclear import and export rates of mCherry, YAP1, YAP1 mutants, and TAZ. We show that import
94 and export rates, despite the wide intercellular variability, are correlated within the same cell, and
95 that the export rate is the main determinant of wild-type YAP1 distribution. Finally, we provide the
96 proof of principle that multiple proteins can be recorded simultaneously within the same cell by
97 analysing YAP1 and TAZ nuclear transit rates.

98

Results

To establish an optogenetic system for protein shuttling studies, we adapted the LOV-TRAP system (Wang and Hahn, 2016, Wang et al., 2016a). With this tool, a mitochondria-tethered LOV domain interacts with its binding partner Zdk98 (Zdk hereafter), fused to the POI labelled with a fluorescent marker. Upon blue-light illumination, LOV and Zdk dissociate, releasing the POI into the cytoplasm within a fraction of a second and enabling subsequent monitoring. We selected the outer surface of mitochondria for sequestration because their distinctive and discrete morphology is well suited to image segmentation. Furthermore, the outer membrane is directly in contact with a large area of the cytoplasm. Therefore, we fused the LOV domain to the mitochondrial anchor sequence TOM20, while the POI was fused to a Zdk peptide sequence. The fluorophore mCherry was selected to visualise the target protein because it is excited with sufficiently long wavelength light to exclude the possibility of triggering a conformational change in the LOV domain. Fig. 1A and Fig. S1B shows a schematic diagram of the constructs and their expected localisation, and expected response to blue light inducing a conformational change in the LOV domain.

An opto-release system for studying nuclear cytoplasmic shuttling

We began by testing if a fusion of the Zdk peptide to mCherry was capable of localising the fluorescent protein to mitochondria in the presence of the TOM20-LOV protein. Cells expressing histone H2B-mTurquoise fusion were co-transfected with these constructs and additionally labelled with a MitoTracker™ dye to allow visualisation of the different compartments. Fig. 1B shows that this approach labels the nucleus and mitochondria in the expected way. Importantly, Zdk-mCherry exhibited expected enrichment to mitochondria in the presence of the TOM20-LOV fusion (Fig. 1B and Fig. S1C, where we show localisation without sequestration). All the constructs used in this study have expected localisation, size and transcriptional activity without sequestration, confirming that these parameters were not affected by fusion with Zdk and mCherry (Fig. S1D-F). We next investigated the effect of 458 nm light illumination. Fig. 1B shows that blue light illumination led to reduced mitochondrial localisation and increased Zdk-mCherry in both the cytoplasm and nucleus. Upon cessation of illumination, the Zdk-mCherry fusion exhibited a progressive transition back to the mitochondria. Quantification of the fluorescent signal in mitochondrial, cytoplasmic, and nuclear compartments confirmed the release and re-binding of Zdk-mCherry to the mitochondria, illustrated in Fig. 1C. Of note, the rate of fluorescence increase and decrease in the nucleus was much slower than that in the cytoplasm. This is most likely

132 related to the rate of nuclear entry and exit of Zdk-mCherry being slower that the kinetics of
133 release and re-binding of the Zdk peptide to the LOV domain. We reasoned that this difference
134 could be exploited to gain quantitative information about the rates of nuclear import and export of
135 proteins. To this end, we developed a computational tool for automatically segmenting the
136 mitochondria, nuclear, and peri-nuclear cytoplasm excluding mitochondria. The time series data
137 generated for each compartment (Fig. 1C) was then fitted to a series of ordinary differential
138 equations (ODEs) (Fig. 1D), with a workflow demonstrated in Fig. 1E.

139

140 **Supervised semi-automated segmentation of cellular compartments using a MATLAB app**
141 To accurately extract quantitative information about the localisation of the fluorescent Zdk-fusion,
142 we developed a supervised MATLAB app for thresholding the different cellular compartments.
143 Upon loading the imaging data and defining the appropriate channels (Fig. S2A), the region
144 containing the cell of interest can be selected. Percentile intensity projections of all frames in each
145 relevant channel are made at levels appropriate to bring out the features of each compartment
146 whilst minimising noise and interference from neighbouring cells (Fig S2A). The percentile
147 projections are then thresholded to define appropriate compartment boundaries. The appropriate
148 threshold for identifying the whole cell is then set using a sliding tool that provides a real-time
149 image of the result of the thresholding (Fig. S2C). Once an appropriate value has been selected,
150 the process is repeated for the thresholding of the mitochondria, and then the nucleus (Fig. S2D).
151 In the analysis presented here, nuclear segmentation was based on the fluorescent histone image
152 and mitochondrial segmentation was based on MitoTracker™. Thresholding of the cytoplasmic
153 compartment was used to define a region around the nucleus, with mitochondrial regions
154 automatically excluded. We typically chose a threshold that excluded thinner parts of the cell
155 periphery that did not fill the whole z-plane being acquired. Once thresholds are set, the app
156 generates both visual plots and a numerical data file to allow model fitting and the estimation of
157 rates of binding and unbinding of the fluorescent Zdk fusion protein from mitochondria and its
158 rates of nuclear entry and exit (Fig. S2D).To account for possible changes in the intensity of
159 fluorescent cellular, nuclear, and mitochondrial labels during the imaging, the thresholding
160 parameters could be re-defined at varying points during the time series. The result of this dynamic
161 thresholding could then be compared with constant threshold values, with the method giving
162 smaller errors in fitting selected for subsequent quantitative analysis.

163

164 **Differential equations to model nuclear import and export**

165 Having generated numerical data of the localisation of Zdk-fusion protein of interest over time, we
166 then sought to determine the rates of nuclear entry and exit. We used ODEs to model this as a
167 system with three key variables: the amount of Zdk-fusion bound to mitochondria, the amount in
168 the cytoplasm, and the amount in the nucleus (Fig. 1D). Transitions were permitted from the
169 mitochondria to the cytoplasm, and vice-versa, and from the cytoplasm to the nucleus, and vice-
170 versa. The rate of transition on and off mitochondria and rates from cytoplasm to nucleus and
171 nucleus to cytoplasm transfer were fitted simultaneously from the system of ODEs. To account
172 for any photobleaching, we applied a normalisation method to ensure that the total level of
173 fluorescence was constant over time. This improved the data fitting.

174 Fig. 1F,G show the directly measured mitochondrial release and re-binding rates and the inferred
175 rates of Zdk-mCherry nuclear entry and exit. As we expected, the rates of transit on and off the
176 mitochondria were considerably faster than the nuclear transit rates (compare Fig. 1F with
177 "Optorelease" samples in Fig. 1G). Our methodology uses information from both the release and
178 re-binding phases of the experiment to determine the nuclear entry and exit rates. Fig. S3A,B
179 shows the advantage that this confers over using only the release or only the re-binding phase,
180 with two-fold and eight-fold reductions in the intervals of plausible fitted parameter values when
181 both release and re-binding phases are used compared to release and re-binding phases,
182 respectively. We sought to corroborate the rates of nuclear entry and exit using a conventional
183 fluorescence loss in photobleaching method (FLIP). In this method, we continuously deplete the
184 Zdk-fluorescence at a location either in the cytoplasm (cytoFLIP) or the nucleus (nucFLIP) and
185 record the diffusion of bleached fluorophore in the other compartment. Fig. 1G shows good
186 concordance between the rates measured using our opto-release method and cytoFLIP. Of note,
187 if we performed nucFLIP with continuous bleaching at a point in the nucleus, then the rates of
188 nuclear entry and exit diverged from those measured using both cytoFLIP and opto-release. More
189 specifically, the inferred rates were faster. This is most probably due to direct photobleaching of
190 the fluorophore in the cytoplasm above and below the nucleus. This highlights an important caveat
191 of FLIP experiments – namely the choice of photobleaching location.

192

193 **Application of opto-release methodology to YAP1 and TAZ**

194 Having established that our method involving light-dependent release of a molecule from
195 sequestration on the outer surface of mitochondria was capable of measuring nuclear entry and
196 exit rates, we applied our method to measure the nuclear import and export rates of the

197 transcriptional regulators YAP1 and TAZ. YAP1 and TAZ were fused to the Zdk peptide and
198 mCherry. Fig. S1E confirms that these chimeric proteins retained their expected ability to drive
199 transcription from a TEAD-dependent promoter, indicating that fusion with fluorophore and Zdk
200 peptide didn't affect binding to other proteins. As before, blue light was used to release YAP1 and
201 TAZ from sequestration and their redistribution into the cytoplasm and nucleus was tracked. After
202 600 seconds, the blue light illumination was stopped and the return of signal to the mitochondria
203 was monitored (Fig. 2A). The app interface described above was then used to extract quantitation
204 (Fig. 2B,C) that was then fitted to the model (Fig. 2D-H). These analyses reveal that both YAP1
205 and TAZ have slightly lower mitochondria release/recovery rates (Fig. 2D-F), but elevated nuclear
206 import and export rates compared to mCherry, with TAZ rates being slightly faster than the rates
207 of transit across the nuclear envelope for YAP1 (Fig. 2G,H). Once again, we confirmed that
208 measurements obtained by optogenetic release and re-sequestration of YAP1 agreed with data
209 obtained using more conventional FLIP methodology (Fig. S4A-I).

210

211 **Active YAP1 is subject to reduced rates of nuclear export**

212 Compartmentalization of YAP1 and TAZ is regulated by different post-translational modifications
213 and, despite recent evidences on the importance of methylation and acetylation, the most
214 characterised is phosphorylation. YAP1 and TAZ are negatively regulated by LATS1/2-dependent
215 phosphorylations, downstream of the Hippo pathway, and conversion of these residues to alanine
216 generates a LATS1/2-insensitive YAP1_5SA mutant that shows nuclear localisation and higher
217 transcriptional activity. On the contrary, the YAP1_S94A mutant is transcriptionally inactive and
218 accumulates in the cytoplasm, due to its inability to bind the transcriptional cofactor and nuclear
219 tether TEAD. We investigated if YAP1_5SA and YAP1_S94A mutants exhibited different nuclear
220 import and export rates. Fig. 3A-C and Fig. S5A-E show that the most prominent effect of 5SA
221 mutations is reduced nuclear export compared to the wild-type isoform. In contrast, this doesn't
222 hold true for the YAP1_S94A mutant, that shows rates comparable to the wild-type isoform. Rates
223 of nuclear import and export are consistently correlated as shown for YAP1 and its mutants in
224 Fig. 3C. Cells with high rates of YAP1 nuclear import also had high rates of nuclear export. These
225 data suggest that the energetic cost of transit across the nuclear pore might be highly variable
226 between cells, but that this variation in cost applies to both nuclear entry and exit. Furthermore,
227 even though there is considerable inter-cellular variation in the rates, the process remains subject
228 to regulation. These results support our previous findings that YAP1_5SA nuclear persistence
229 can be explained by slower nuclear exit, while cytoplasmic enrichment of S94A at steady state

230 cannot simply explained by regulation of NC shuttling and thus requires additional explanations,
231 such as tethering by cytoplasmic proteins (Ege et al., 2018).

232

233 **Import and export rates are correlated**

234 We were intrigued that the variance in import and export rates spanned an order of magnitude
235 and investigated if this variation might correlate with differences in cell or nuclear morphology, as
236 has been suggested for nuclear import previously (Elosegui-Artola et al., 2017). Fig. 4A-E shows
237 correlation analysis of import and export rates with a range of nuclear morphology parameters.
238 Some correlations are trivial, such as the positive association between area and perimeter,
239 whereas as others are more intriguing, for example, the ratio of import and export rates was
240 strongly correlated with the relative NC distribution. This latter metric reflects the relative
241 segregation of any molecules that were not effectively sequestered by the LOV domain prior to
242 the period of illumination. This is reassuring because in a simple model the ratio between relative
243 rates of import and export should reflect the distribution of molecules between the two
244 compartments at steady state. However, it is not possible to attach too much significance to this
245 as the initial nuclear and cytoplasmic distributions of the fluorophore are assumed to be linearly
246 proportional to the fitted compartment transfer rates and initial mitochondrial intensity in the model
247 fitting. Thus, this observation reflects that our modelling approach is internally consistent. That
248 said, import/export ratio positively correlates with NC distribution for all the proteins analysed,
249 whereas single values of import and export did not, suggesting a biological information beyond
250 the mere technical control. Similarly, import/export ratio positively correlates with nuclear area to
251 cytoplasmic area ratio. Since fitting population intensities, this might reflect that larger nuclei will
252 contain relatively greater levels of fluorescent molecules. Interestingly, the cytoplasmic shape
253 parameters did not show any significant correlations with import and export rates (Fig. S6A-E).
254 More intriguingly, we note that only in the case of YAP1 there was a negative correlation between
255 the export rate and nuclear/cytoplasmic ratio (Fig. 4F). This suggests that tuning of the export
256 rate is the main determinant of the overall nuclear/cytoplasmic distribution of YAP1 and that it
257 becomes reduced as the nucleus takes up a larger area of the cell. Plots relating nuclear import
258 to the same parameters did not show any correlation. The lack of correlation between export rate
259 of mCherry, TAZ, or the YAP1 mutants, with nuclear/cytoplasm ratio or nuclear area/cytoplasmic
260 area indicates that this regulation is specific to wild-type YAP1 and that some mechanisms don't
261 apply to YAP1 mutants (such as cytoskeletal regulation of YAP1_5SA mutant (Ege et al., 2018).

262

263 **Simultaneous measurement of YAP1 and TAZ nuclear transit rates reveals that they are**
264 **correlated**
265 The observation of variance in nuclear transit rates between cells prompted us to wonder if the
266 transit rates of two different proteins in the same cell might be correlated. Testing this idea using
267 conventional FLIP methodology would be highly challenging as it would require both bleaching
268 and imaging two fluorophores simultaneously, with significant potential for unintended bleaching
269 artefacts. However, using the opto-release system with two differently labelled POIs would have
270 fewer problems. Therefore, we labelled YAP1 with Venus and TAZ with mCherry and confirmed
271 that proteins could be tracked in parallel (Fig. 5A). Fig. 5B,C and Fig. S7A-C show that
272 mitochondrial release and nuclear import are similar between YAP1 and TAZ, but the latter shows
273 increased nuclear export (Fig. 5C). This suggests a lower tethering of TAZ in the nucleus
274 compared to YAP1, maybe due to the relative contribution of different mechanisms, such as YAP1
275 regulation by the cytoskeleton (Dupont et al., 2011, Calvo et al., 2013) and the presence of
276 different NLS and NES sequences in YAP1 and TAZ (Kofler et al., 2018, Fang et al., 2018).
277 Importantly, both export and import rates of YAP1 significantly correlate with those of TAZ,
278 indicating still a large overlap between the mechanisms regulating NC shuttling of the two proteins
279 (Fig. 5D,E).

280

281 **Implementation of opto-release methodology on lattice lightsheet platform**

282 YAP1 and TAZ can be associated with a wide array of binding partners in diverse sub-cellular
283 compartments. Confocal analysis of a single optical section is not suited analyzing the distribution
284 of molecules throughout the cell. Therefore, we sought to implement our opto-release method on
285 a lattice lightsheet microscope with suitable laser lines for the release of the Zdk peptide from the
286 LOV domain. The experimental design was adapted from the simple release and re-binding
287 protocol, with additional single frames of blue light included at 80 second intervals in the re-binding
288 phase (Fig. 6A). The additional blue light pulses were to explore if events with different kinetics
289 might also be observed when the whole cell volume was acquired with high spatial resolution
290 (104nm xy and 211nm z resolution). Fig. 6B shows 3D image of confluent HaCaT cells, with one
291 expressing the Zdk-mCherry-YAP1 construct. As expected, the Zdk-mCherry-YAP1 fusion
292 exhibits efficient localization to the mitochondrial network in frame 1, but is widely distributed
293 throughout the cell by frame 80/480 seconds (3D view shown in Fig. 6C and xy, xz, yz orthogonal
294 slices shown in Fig. S8A,B). Following the end of the long phase of blue light illumination, the
295 YAP1 fusion returns to the mitochondria (Fig. 6C – 556 seconds). As expected, this localization

296 is diminished immediately following the pulses of blue light at 560, 640, and 720 seconds (Fig. 6D
297 left-hand panel). Quantification of the Zdk-mCherry-YAP1 signal from representative areas of the
298 cytoplasm, and nucleus are shown in Fig. 6D. These traces clearly show the pulsatile release of
299 the YAP1 fusion into the cytoplasm, but this does not translate into changes in nuclear signal.

300 The purpose of performing high resolution lattice light sheet imaging was to determine if the
301 dynamics of the YAP1 fusion protein might be varying depending on the precise subcellular
302 localization. We therefore quantified multiple cytoplasm and nuclear regions. Interestingly,
303 different regions showed markedly divergent kinetics. Despite the whole cell being illuminated
304 with short pulses of blue light, the extent of gain in YAP1 signal and its duration appeared to vary
305 from region to region. Some areas had a pronounced increase that decayed sharply (regions
306 1&5), while in other parts of the cytoplasm the increase was less pronounced, but more durable
307 (regions 2&3), or barely detectable at all (Fig. 6E – similar data for the cytoplasm of a different
308 cell is shown in Fig. S8C). Differences were also observed in the shape of the nuclear intensity
309 profiles (Fig. S8D). To more rigorously explore the differences between cytoplasmic regions we
310 exploited the fact that there were three equal duration pulses in the time series data. Therefore,
311 we considered each pulse to be a 'technical replicate' and derived the average response for the
312 difference cytoplasmic regions. Fig. 6F shows the difference in the average responses, with
313 statistically significant differences in peak intensity and the rate of signal decline after the peak
314 shown in Fig. S8E. Furthermore, a low maximal intensity post-blue light pulse correlative with a
315 slower decay of signal; these data are consistent with slower movement of YAP1 both into and
316 out of these regions. These data demonstrate that YAP1 dynamics vary between different regions
317 of the cytoplasm and illustrate the utility of combined optogenetic manipulation and lattice
318 lightsheet imaging for studying sub-cellular variation in protein dynamics.

319

320 ## Discussion

321

322 Decoding the complex regulatory inputs governing the NC distribution of proteins requires
323 accurate measurement of rates of nuclear entry and exit. During the last decade, several works
324 showed that on YAP1 and TAZ converge an incredibly large number of different signals, from
325 cellular architecture and microenvironment geometry to metabolic and biochemical pathways
326 (Pocaterra et al., 2020). Here, we implement an optogenetic system to track the NC shuttling of
327 fluorescent YAP1 and TAZ proteins coupled to mathematical modeling to derive nuclear

328 import/export rates. This system builds upon the previously reported LOV-TRAP optogenetic tool
329 that allows protein dissociation within a fraction of a second upon illumination with blue light (450-
330 490 nm). In our system, which we term 'opto-release', we exploited the light-induced dissociation
331 of the LOV domain tethered on mitochondria surface from a previously identified synthetic peptide
332 (Zdk) fused to YAP1 or TAZ and then monitor their sub-cellular distribution over time. With this
333 system we can rapidly generate a pool of fluorescently labeled cytoplasmic YAP1 and TAZ that
334 can be tracked in the cell after release from mitochondria (light) and recovery (dark). The LOV-
335 TRAP system has several advantages over other optogenetic systems for this purpose: i) Zdk is
336 a small peptide and doesn't interfere with endogenous activity of YAP1 and TAZ (as shown in Fig.
337 S1E); ii) the LOV domain utilizes an endogenous chromophore (flavin mononucleotide), reducing
338 external intervention during analysis; iii) it allows the study of multiple fluorescently-labeled
339 proteins with sufficient spectral separation, such as mCherry and Venus (Fig. 5); and iv) it allows
340 rapid, reversible and non-destructive analysis compared to FLIP, thus allowing repeated cycles
341 of light-dark and generation of three curves, from release and recovery dynamics leading to more
342 precise measurements.
343
344 Using our opto-release system, we measure YAP1 and TAZ shuttling rates. Despite being larger
345 than mCherry, both YAP1 and TAZ shuttle in and out of the nucleus faster, with roughly 10% of
346 TAZ entering or exiting the nucleus every second. This indicates active mechanisms of both
347 import and export. The rate of YAP1 transit that we measure in epithelial HaCaT cells is similar
348 to that which we previously reported for YAP1 in fibroblasts using FRAP and FLIP methodology
349 (Ege et al., 2018). Direct comparison of opto-release with FLIP methods in HaCaT cells showed
350 good concordance when the photobleaching was performed in the cytoplasm. The discordant
351 results of nuclear photobleaching are probably due to direct photobleaching of fluorophore in the
352 cytoplasmic regions of the cell directly above and below the nucleus. The greater height and more
353 cuboidal nature of epithelial cells, such as HaCaT, compared to fibroblasts mean that there will
354 be more cytoplasm above and below the nucleus. This will lead to greater levels of photobleaching
355 occurring directly in the cytoplasm during nuclear FLIP experiments and will confound the results.
356
357 In our analysis, mutation of LATS phosphorylation target sites on YAP1 leads to reduced nuclear
358 export that can explain YAP1_5SA nuclear accumulation (Fig. 3B), which is consistent with LATS-
359 mediated phosphorylation being required for effective export (Ege et al., 2018). Intriguingly, the
360 YAP1_S94A mutant, which is unable to bind TEAD, is localized in the cytoplasm at steady-state,
361 and in our analysis its import/export rates are close to those calculated for YAP1_WT (Fig. 3A,B)

362 even though it is more cytoplasmic than the wild-type YAP1. This could be explained if there is a
363 pool of YAP1 that remains sequestered in the cytoplasm with binding and unbinding rates that
364 are too slow to measure in the few minutes duration of our assays. Indeed, several studies have
365 suggested cytoplasmic partners for YAP1 (Kanai et al., 2000, Azzolin et al., 2014, Varelas et al.,
366 2010, Zhao et al., 2010). In the future, it will be interesting to perform longer release phase
367 experiments with a view to the released YAP1 reaching equilibrium distribution in all sub-cellular
368 compartments. Although we focused exclusively on NC distribution in our study, the opto-release
369 system could equally be applied to problems involving the segregation of proteins between
370 different cytoplasmic compartments: for example, the plasma membrane and cytoplasm. The
371 mathematical modelling of spatial information in addition to temporal information using partial
372 differential equations as in Ege et al. (Ege et al., 2018) will also allow us to separate import and
373 export from motility within each compartment.
374
375 Interestingly, we could confirm that import and export rates are correlated within the same cell,
376 but show high intercellular variability, as observed in Drosophila (Manning et al., 2018). Our
377 conclusion that nuclear export is the main mechanism for the regulation of YAP wild-type activity
378 differs from evidence in *Drosophila*, where Yorkie is mainly regulated by tuning nuclear import
379 (Manning et al., 2018). A possible explanation for this discrepancy is that Yorkie (the *Drosophila*
380 homologue of YAP1), lacks PDZ-binding motif that is required for the nuclear accumulation of
381 YAP1 in mammals (Wang et al., 2016b, Oka and Sudol, 2009). By releasing two proteins
382 simultaneously, we could also show that YAP1 and TAZ import and export rates co-varied
383 indicating that they share some regulatory inputs, with LATS-mediated phosphorylation being an
384 obvious candidate. However, we also found evidence for some specificity in regulation between
385 YAP1 and TAZ. For example, wild-type YAP1 export rate negatively correlates with NC ratio,
386 supporting the idea that the rate of nuclear export may be tuned in response to variation in
387 morphological features of the cell, but this was not true for TAZ. It was also not true for YAP1_5SA,
388 which is at least consistent with our previous finding that cytoskeletal inputs primarily tune the
389 export rate of phosphorylated YAP1. Thus, while YAP1 and TAZ share to some extent
390 mechanisms of NC shuttling, specific regulations are in place, as shown by a recent study on
391 TAZ-specific NES/NLS sequences (Kofler et al., 2018). Of note, FRAP early experiments with
392 GFP-TAZ showed that TEAD-binding defective TAZ mutants exhibit higher nuclear export (Chan
393 et al., 2009). Despite correlation of import/export with several morphological metrics, we couldn't
394 observe a link between NC shuttling and nuclear deformation, as reported in Elosegui-Artola et

395 al. (Elosegui-Artola et al., 2017). However, we did not apply any direct or indirect perturbations to
396 the nuclear envelope.
397
398 Current FRAP and FLIP methodologies are routinely employed with a focus on a single optical
399 plane of the cell. This is partly due to the difficulties in obtaining multiple optical sections with the
400 necessary speed and partly due to the difficulties accounting for the changes in the size and
401 intensity of the photobleaching region as a function of distance in the z-dimension. However, opto-
402 release technology does not suffer from the variation in photobleaching as a function of z position,
403 especially if the whole cell is illuminated. Furthermore, advances in lattice lightsheet technology
404 now allow for the rapid acquisition of high resolution volumetric data of whole cells. Therefore, we
405 implemented our opto-release methodology on a lattice lightsheet platform. This revealed
406 additionally complexity in the behavior of the Zdk-mCherry-YAP1 fusion in different regions of the
407 cytoplasm, with some regions showing rapid increases and decreases in signal following a pulse
408 of blue light and other regions showing lower peak intensities and slower decreases in signal. The
409 regions with slower kinetics may reflect areas with slow diffusion or slow binding to a tethered
410 partner molecule. In the future, it will be interesting to characterize these different regions by co-
411 staining for other organelles and YAP1 binding partners. These differences also highlight the
412 limitations of applying a simple mathematical model that only considers mitochondrial,
413 cytoplasmic, and nuclear compartments with no locally varying properties or sub-compartments.
414 This is likely a source of uncertainty or error in our fitting of import and export rates. Nonetheless,
415 ODE modelling of the predicted YAP1 levels in different cellular compartments under the blue
416 light regimen used in the lightsheet experiments was consistent with the observed changes in
417 mitochondrial and nuclear Zdk-mCherry-YAP1 signal, and with cytoplasm regions 1 and 5
418 (compare Fig. S8F and Fig. 6E). The modelling also predicts that short pulses of blue-light would
419 have only a minimal effect on nuclear intensity. The smaller magnitude of changes in the nucleus
420 mean that the experimental data are noisier, nonetheless, they support the prediction of minimal
421 effect of the blue-light pulses on nuclear YAP1 levels. Solving the issue of heterogenous YAP1
422 dynamics in the cytoplasm will require a more complex model with a larger number of
423 compartments and more spatial features. It will also require implementation of 3D segmentation
424 tools for different cellular compartments.
425
426 In the present study, we report the use of a reversible optogenetic system based upon the LOV-
427 TRAP system (Wang and Hahn, 2016, Wang et al., 2016a). This methodology allows controlled
428 release of fluorescent proteins that can be tracked over time in the different cell compartments.

429 The reversibility of the optical release enables more complex experimental design than is possible
430 with conventional FRAP and FLIP analyses. In particular, by varying the timing and length of
431 release and re-binding phases it is possible to acquire data about processes happening with
432 different timescales in the same experiment. Alternatively, repetitive use of a signal illumination
433 pulse or sequence can effectively generate 'technical replicates' in a single experiment, leading
434 to more accurate measurements. We generated a MATLAB app for thresholding of different
435 cellular compartments and compensation of cell motion. This tool then extracts numerical values
436 for NC localization that are used by differential equations to generate import/export rates. While
437 we have used this system to gain further insights in YAP1 and TAZ NC shuttling, the modular
438 nature of the constructs will make it easy to adapt to a range of transcription factors and
439 regulators, including SMADs, NF-kB, MRTF, IRFs, and STATs. We anticipate that opto-release
440 systems based on this framework will facilitate the understanding of how diverse inputs regulate
441 the sub-cellular localization of proteins and will be of wide utility to cell biologists.
442

443 ## Figure legends

444

445 **Figure 1: Opto-release system.**

446 **(A)** Opto-release system specifications; In the dark, Zdk-tagged protein is tightly sequestered on
447 the mitochondria through the interaction with light sensitive LOV domain. The LOV domain is
448 tethered to the mitochondria through TOM20 protein anchor. Upon blue light illumination, the LOV
449 domain changes conformation and releases Zdk-tagged protein.

450 **(B)** Representative image of Zdk-flag-mCh constructs release and recovery from mitochondrial
451 sequestration by TOM20-flag-LOVwt. Experiment with 10 min of blue light illumination (the
452 release phase), followed by 10 min of dark recovery without blue light (the recovery phase). Scale
453 bar is 10μm.

454 **(C)** Quantification of intensities corresponding to optogenetic release and recovery experiment
455 performed in HaCaT cells transiently transfected with Zdk-flag-mCherry (n=15 cells). Only the
456 mean of all cells from at least 3 biological replicates is shown for clarity. Intensity has been
457 corrected for bleaching and background signal.

458 **(D)** System of ordinary differential equations used to derive the shuttling rates of import, k_{imp},
459 export, k_{exp}, rate of mitochondrial release, K_{rel}, and rate of mitochondrial recovery, k_{rec} for the
460 nucleus, $n(t)$, cytoplasm, $c(t)$ and mitochondria, $m(t)$ at time t. The function $\phi(t)$ allows the fitting
461 of the escape of intensity to elsewhere in the cell.

462 **(E)** Experimental pipeline. Confocal imaging is followed by semi-automated intensity thresholding
463 and shuttling rate analysis with mathematical modelling.

464 **(F)** The numerical values of mitochondrial sequestration rates at steady state (darkness), during
465 release and during recovery phases, compared to nuclear import/export rates for Zdk-flag-
466 mCherry (n=16), Number of cells is given in brackets. Boxplot (10&90 percentile, median)
467 represents at least three independent biological replicates. Mann-Whitney U test.

468 **(G)** Zdk-flag-mCherry nuclear import and export rates acquired using nuc/cyto FLIP method
469 compared to the optogenetics method. Boxplot (10&90 percentile, median) represents at least
470 three independent biological replicates. The values of optogenetic-derived import/export rates
471 from G are replotted here for clarity and comparison to FLIP. Mann-Whitney U test.

472

473 **Figure 2: Rates of YAP1 and TAZ nucleocytoplasmic shuttling in HaCaT epithelial cell line.**

474 **(A)** Representative images of Zdk-flag-mCh-YAP1_WT/TAZ constructs release and recovery
475 from mitochondrial sequestration by TOM20-flag-LOVwt. Experiment with 10 min of blue light

476 illumination (the release phase), followed by 10 min of dark recovery without blue light (the
477 recovery phase). Scale bar is 10μm.
478 **(B)(C)** Quantification of absolute intensities corresponding to optogenetic release and recovery
479 experiment performed in HaCaT cells transiently transfected with (B) Zdk-flag-mCh-YAP1_WT
480 (n=24) or (C) Zdk-flag-mCh-TAZ (n=22). Only the mean of all cells from at least 3 biological
481 replicates is shown for clarity. Intensity has been corrected for bleaching and background signal.
482 **(D)(E)(F)** The numerical values of mitochondrial sequestration rates for Zdk-flag-mCherry-
483 YAP1_WT (n=28) and Zdk-flag-mCh-TAZ (n=22) in steady state (darkness), during release and
484 during recovery phases. Number of cells per each condition is given in brackets. Boxplot (10&90
485 percentile, median) represents at least three independent biological replicates. Mann-Whitney U
486 test.
487 **(G)(H)** YAP1 and TAZ nuclear import and export rates. Boxplot (10&90 percentile, median)
488 represents at least three independent biological replicates. Mann-Whitney U test.
489
490 **Figure 3: Rates of YAP1 mutants nucleocytoplasmic shuttling in epithelial cell line.**
491 **(A)(B)** YAP1 mutants nuclear import and export rates. Boxplot (10&90 percentile, median)
492 represents at least three independent biological replicates. Mann-Whitney U test.
493 **(C)** Scatterplot of import versus export and line of the best fit for Zdk-flag-mCherry-YAP1_WT
494 (teal), Zdk-flag-mCherry-YAP1_5SA (dark blue), Zdk-flag-mCherry-YAP1_S94A (orange).
495
496 **Figure 4: Nuclear morphology correlation with import and export.**
497 **(A)(B)(C)(D)(E)** Import and export correlations with nuclear morphology, specified by area,
498 perimeter, circularity and eccentricity, as well as nuclear-to-cytoplasmic ratio and nuclear area as
499 proportion of cell. Plots show Zdk-flag-mCherry (A), Zdk-flag-mCh-YAP1_WT (B), Zdk-flag-mCh-
500 YAP1_5SA (C), Zdk-flag-mCh-YAP1_S94A (D) and Zdk-flag-mCh-TAZ (E). Circle colour reflects
501 Pearson correlation (bright red +1, dark blue -1) and circle size the p-value of the correlation
502 (large, significant; small, nonsignificant).
503 **(F)** Negative correlation between export and NC ratio of YAP1_WT.
504
505 **Figure 5: Rates of YAP1 and TAZ in the same cell.**
506 **(A)** Representative images of release and recovery experiment in Zdk-flag-Venus-YAP1_WT and
507 Zdk-flag-mCh-TAZ using a two-colour optogenetics setup. Scale bar is 10 μm.

508 **(B)(C)** YAP1 and TAZ nuclear import and export rates in the same cell. Boxplot (10&90 percentile,
509 median) represents at least three independent biological replicates. Wilcoxon matched-pairs
510 signed rank test.
511 **(D)(E)** Scatterplot of YAP1 versus TAZ import (D) or export (E) rates in the same cell. Pearson
512 coefficient (r) and significance (p-value) are also shown.
513
514 **Figure 6: YAP1 dynamics in 3D.**
515 **(A)** Schematic representation of lattice lightsheet imaging experimental design.
516 **(B)** Representative image of HaCat cell expressing Zdk-flag-Venus-YAP1_WT imaged on lattice
517 lightsheet microscope. Scale bar is 10 µm.
518 **(C)** Release and recovery experiment of Zdk-flag-Venus-YAP1_WT in 3D. Scale bar is 5 µm.
519 **(D)** Quantification of intensities corresponding to optogenetic release and recovery experiment
520 performed in HaCaT cell expressing Zdk-flag-Venus-YAP1_WT in 3D. The curves show the
521 average intensities in selected regions of the mitochondria, the cytoplasm and the nucleus.
522 **(E)** Quantification of intensities corresponding to different cytoplasmic regions during the 3D
523 optogenetic experiment in HaCaT cell expressing Zdk-flag-Venus-YAP1_WT.
524 **(F)** Average post-blue light spike intensity profiles for different cytoplasmic regions in HaCaT cell
525 expressing Zdk-flag-Venus-YAP1_WT.
526
527 **Supplementary Figure 1: Related to Figure 1. Localization, expression and function of**
528 **unsequestered Opto-release constructs.**
529 **(A)** Schematic of main known mechanisms of regulation of YAP1 and TAZ.
530 **(B)** Schematic of various constructs used for opto-release system.
531 **(C)** Representative images of HaCaT cells expressing CMV-driven Zdk constructs (transient
532 transfection). Actin is presented in green, DAPI in magenta and mCherry in greyscale. Scale bar
533 is 50 µm.
534 **(D)** Boxplot (10&90, median) of nuclear-to-cytoplasmic ratio (log2 scale) corresponding to three
535 experimental repeats of HaCaT cells transiently transfected with CMV-driven Zdk constructs
536 (n>29cells; n>20 for Taz, 2 experimental repeats). Mann-Whitney U test.
537 **(E)** Expression of unsequestered Zdk constructs. Western blot showing expression of Opto-
538 release constructs stably expressed in HaCaT cell line. Empty arrowheads point to Opto-release
539 protein (Zdk-flag-mCh 37.5kDa, Zdk-flag-mCh-YAP1_WT 96kDa, Zdk-flag-mCh- TAZ_WT
540 85kDa) and filled arrowheads point to endogenous protein (YAP1 70kDa, TAZ 50kDa). An arrow

541 points to a cleavage product. Anti-RFP antibody recognizes mCherry fluorescent protein.
542 [Symbol]-tubulin as loading control (42kDa) is also presented.
543 **(F)** Luciferase assay using TEAD-driven reporter (5xMCAT) for YAP1/TAZ activity in HaCaT cells
544 following transient transfection with Zdk constructs driven by CMV promoters. Boxplot (10&90,
545 median) represents three independent experiments, each with 3 technical replicates. Mann-
546 Whitney U test, statistics above each bar represent comparison to MCH negative control.
547
548 **Supplementary Figure 2: Related to Figure 1. Image analysis pipelines.**
549 **(A)** MATLAB app showing user input and channel selection tab. **(B)** MATLAB app showing user
550 determined percentile projections for each channel in the central panel. Here, the percentile for
551 the whole cell is too high, leading to high noise and interference from neighbouring cells. The
552 nuclear channel's percentile is too low, leading to no obvious nuclear object. The percentile for
553 the mitochondrial channel is close to optimum. The right-hand panel illustrates population intensity
554 profiles and segmentation information for a single window split. **(C)** MATLAB app showing, in the
555 central panel, how the threshold value to segment the whole cell can be altered. The right-hand
556 panel shows population intensity output and relevant parameter values for the movie split into a
557 single window (blue), two windows (cyan) and the first window of a four window split (yellow). **(D)**
558 MATLAB app showing the segmentation of the nucleus and mitochondria in the central panel and
559 further population intensity output and relevant parameter values for one (blue), two (cyan) and
560 four (yellow) window splits in the right-hand panel. Changes in thresholding in the central panel
561 will change the intensity profiles of the third quarter of the yellow signal (four window split) in real
562 time. The intensity profile of the nucleus is higher in this quarter than the one preceding it,
563 suggesting that the nuclear threshold should be higher.
564
565 **Supplementary Figure 3: Related to Figure 2. Analysis of uncertainty of parameter values**
566 **for release fit, recovery fit or release + recovery fit.**
567 **(A)(B)** Frequency distributions of import (A) and export (B) values that produce fits with sum of
568 squares of error at most twice that of the global optimum when varying import and export
569 simultaneously. The dots show the location of optimum fit and suggest release-only fitting
570 underestimates both import and export while recovery-only overestimates import and export. All
571 other parameter values were fixed at their global optimums. Size of distribution shows greatest
572 certainty with release and recovery and least with only recovery.
573
574

575 **Supplementary Figure 4: Related to Figure 2. Confirmation of shuttling rates using FLIP.**
576 **(A)(B)(C)** Nuclear FLIP analysis of unsequestered Zdk-mCherry constructs. Quantification of
577 absolute intensities normalized to control cell and background intensity, corresponding to FLIP
578 experiment performed in the nucleus of HaCaT cells transiently transfected with (A) Zdk-flag-
579 mCherry (n=32 cells, 4 biological replicates), (B) Zdk-flag-mCh-TAZ (n=17 cells, 3 biological
580 replicates), (C) Zdk-flag-mCh-YAP1_WT (n=21 cells, 3 biological replicates). Only the mean of all
581 cells is shown for clarity.
582 **(D)(E)(F)** Cytoplasmic FLIP analysis of unsequestered Zdk-mCherry constructs. Quantification of
583 absolute intensities normalized to control cell and background intensity, corresponding to FLIP
584 experiment performed in the cytoplasm of HaCaT cells transiently transfected with (D) Zdk-flag-
585 mCherry (n=22 cells, 3 biological replicates), (E) Zdk-flag-mCh-TAZ (n=22 cells, 3 biological
586 replicates), (F) Zdk-flag-mCh-YAP1_WT (n=20 cells, 3 biological replicates). Only the mean of all
587 cells is showed for clarity.
588 **(G)(H)** YAP1 and TAZ nuclear import and export rates acquired using FLIP methods. The
589 numerical values of nuclear import (k_{imp}) and export (k_{exp}) rates for Zdk-flag-mCherry, Zdk-flag-
590 mCh-TAZ, Zdk-flag-mCh-YAP1_WT are shown. Boxplot (10&90 percentile, median) represents
591 at least 3 independent biological replicates. Mann-Whitney U test.
592 **(I)** Table comparing medians of shuttling rates derived using Opto-release method, FLIP nucleus
593 and FLIP cytoplasm.
594
595 **Supplementary Figure 5: Related to Figure 3. YAP1 mutants parameters.**
596 **(A)(B)** Quantification of absolute intensities corresponding to optogenetic release and recovery
597 experiment performed in HaCaT cells transiently transfected with (A) Zdk-flag-mCh-YAP1_5SA
598 (n=24) or (B) Zdk-flag-mCh-YAP1_S94A (n=22). Only the mean of all cells from at least 3
599 biological replicates is shown for clarity. Intensity has been corrected for bleaching and
600 background signal.
601 **(C)(D)(E)** The numerical values of mitochondrial sequestration rates for Zdk-flag-mCherry-
602 YAP1_5SA (n=14) and Zdk-flag-mCherry-YAP1_S94A (n=12) compared to Zdk-flag-mCherry-
603 YAP1_WT reproduced from Figure 2 (n=28), in steady state (darkness), during release and during
604 recovery phases. Number of cells per each condition is given in brackets. Boxplot (10&90
605 percentile, median) represents at least three independent biological replicates. Mann-Whitney U
606 test.
607

Supplementary Figure 6: Related to Figure 4. Cytoplasm morphology correlation with import and export.

(A)(B)(C)(D)(E) Import and export correlations with cytoplasmic morphology, specified by area, perimeter, circularity and eccentricity. Plots show Zdk-flag-mCherry (A), Zdk-flag-mCh-YAP1_WT (B), Zdk-flag-mCh-YAP1_5SA (C), Zdk-flag-mCh-YAP1_S94A (D) and Zdk-flag-mCh-TAZ (E). Circle colour reflects Pearson correlation (bright red +1, dark blue -1) and circle size the p-value of the correlation (large, significant; small, nonsignificant).

Supplementary Figure 7: Related to Figure 5. Rates of YAP1 and TAZ in the same cell.

(A)(B)(C) The numerical values of mitochondrial sequestration rates for Zdk-flag-Venus-YAP1_WT and Zdk-flag-mCherry-TAZ (n=14 cells) compared in the same cell in steady state (darkness), during release and during recovery phases. Number of cells per each condition is given in brackets. Boxplot (10&90 percentile, median) represents at least three independent biological replicates. Wilcoxon matched-pairs signed rank test.

Supplementary Figure 8: Related to Figure 6. YAP1 dynamics in 3D.

(A)(B) Orthogonal views of HaCaT cell expressing Zdk-flag-Venus-YAP1_WT fusion during recovery (A) and release (B). Scale bar is 10 μm.

(C) Quantification of intensities corresponding to different nuclear regions during the 3D optogenetic experiment in HaCaT cell expressing Zdk-flag-Venus-YAP1_WT.

(D) Quantification of intensities corresponding to different cytoplasmic regions during the 3D optogenetic experiment in another HaCaT cell expressing Zdk-flag-Venus-YAP1_WT (additional to Fig. 6E). **(E)** Scatter plots of peak amplitude and gradient of decrease from maximum value of each peak for each cytoplasmic region of data in Fig. 6E (left and centre) and scatter plot of amplitude of peaks versus gradient of decrease (right). Peak amplitude approximated by maximum minus minimum signal value. For the gradient of decrease a linear fit was made to all data points after and including the peak value. The gradient provides an approximation to rate of decrease of the peak. Data shows region dependent amplitudes, persistence of peaks and that peak amplitude and persistence of peak are correlated. Statistical tests carried out using one-way ANOVA.

(F) Using the model of Fig 1D to predict functional behaviour of population intensity in the mitochondria, cytoplasm and nucleus for the lightsheet experimental set-up. Parameter values are those fitted to YAP1_WT. Release rate during illumination has been increased by a factor of

641 five to qualitatively match the increase in bleaching rate in the lightsheet data. The predictions
642 show good qualitative agreement with Fig 6D.
643

644 Supplementary Movies

645 Movie 1: Movie shows the first 60 frames (240 seconds) of the blue light illuminated release phase
646 of Zdk-mCherry and the first 60 frames (240 seconds) of the non-illuminated recovery phase.

647 Movie 2: Movie shows the first 50 frames (200 seconds) of the blue light illuminated release phase
648 of Zdk-YAP1-mCherry and the first 50 frames (200 seconds) of the non-illuminated recovery
649 phase.

650 Movie 3: Movie shows the first 50 frames (200 seconds) of the blue light illuminated release phase
651 of Zdk-TAZ-mCherry and the first 50 frames (200 seconds) of the non-illuminated recovery phase.

652 Movie 4: Movie shows 3D image of a HaCaT cell release and recovery experiment on the lattice
653 lightsheet microscope.

654 ## Materials and methods

655

656 ### Cell lines and cell culture

657 HaCaT immortal keratinocyte cells were acquired from the Cell Services Facility at the Francis
658 Crick Institute. H2B-mTurquoise2 was introduced to cells using the PiggyBac transposon system,
659 where the plasmid of interest is transfected together with a transposase plasmid PBase, and was
660 described before (Ege et al., 2018). Cells expressing the construct were selected using
661 Puromycin. All the other plasmids were introduced transiently. Cells were cultured in DMEM
662 (Gibco) with 10% foetal bovine serum (FBS) (PAA Labs) and 1% penicillin-streptavidin (Pen-
663 Strep, Gibco) at 37°C and 5% CO2. The cells were removed from the cell culture dish with 0.1%
664 trypsin and 0.02% versene (both Life Technologies) after washing with PBS (Phosphate buffered
665 saline, 1.5 mM KH2PO4, 8 mM Na2HPO4, 2.7 mM KCl, 137 mM NaCl, pH 7.4). Trypsin was
666 neutralised by addition of cell culture media containing 10% FBS.

667 ### Plasmids

668 All the plasmids generated for the opto-release system were cloned using the Gibson Assembly
669 System (NEB) by combining pRK5.1 backbone with desired PCR fragments according to the
670 manufacturer's instructions. It is based on a previously published LOV-TRAP (Wang and Hahn,
671 2016, Wang et al., 2016a). The photo-switchable modified common oat (Avena sativa) light-
672 oxygen-voltage (LOV) 2 domain from Phototropin 1 protein is fused to TOM20 protein fragment,
673 which embeds it in the outer mitochondrial membrane. On the other side of the system there is
674 the YAP1/TAZ protein, which is joined to Zdk, an engineered small protein domain based on the
675 Z domain described previously (Wang and Hahn, 2016, Wang et al., 2016a), and fluorescent
676 proteins (mCherry or Venus, both photostable in this system and in the timescale of our
677 experiments. YAP1 corresponds to the human YAP1-2γ isoform, which is 504 amino acids long
678 (Sudol, 2013) and the mutants were described before (Ege et al., 2018). The five serines mutated
679 for the 5SA mutant correspond to serines 61, 109, 127, 164 and 397 (=381) for the isoform used
680 in this study. The two plasmids used for the luciferase experiments, pGL3-49 and pGL3-5xMCAT-
681 49, a gift from Nic Tapon. The pPB-puro-H2B-mTurquoise2 was generated in the lab (Ege et al.,
682 2018).

683

Plasmid name	Colours	Promoter	Use	Source
pRK5.1-TOM20-flag-LOVwt	none	CMV	optogenetics	cloned
pRK5.1-Zdk-flag-mCh	mCherry	CMV	optogenetics	cloned
pRK5.1-Zdk-flag-mCh-YAP1_WT	mCherry	CMV	optogenetics	cloned
pRK5.1-Zdk-flag-mCh-YAP1_5SA	mCherry	CMV	optogenetics	cloned
pRK5.1-Zdk-flag-mCh-YAP1_S94A	mCherry	CMV	optogenetics	cloned
pRK5.1-Zdk-flag-mCh-TAZ	mCherry	CMV	optogenetics	cloned
pRK5.1-Zdk-flag-Venus-YAP1_WT	mCherry	CMV	optogenetics	cloned
pGL3-49	luciferase	N/A	luciferase assay	Tapon lab
pGL3-5xMCAT-49	luciferase	N/A	luciferase assay	Tapon lab
pcDNA3-Clover	Clover	CMV	filler plasmid for luciferase assay	Addgene #40259
pGL4.75 CMV-Renilla	renilla	N/A	luciferase assay	Promega, #E6931

684

685 **DNA Transfection.** For transient transfection with plasmid DNA, cells were transfected with
686 Lipofectamine LTX and Plus reagents combination (# 15338100, Thermofisher) according to the
687 manufacturer's instructions. One day prior to the transfection, cells were seeded 0.5-1x 10^6 cells
688 for Western blotting and luciferase transfection in a 6 well plate, or 20 000-100 000 for live
689 imaging and immunofluorescence in a 24 well plate. Prior to transfection media was changed to
690 Pen-Strep free. On the day of transfection two tubes were prepared (proportions below for 24 well
691 plate):

692 Tube 1: 100 µl OptiMEM + 1-2 µg DNA + 2 µl Plus reagent

693 Tube 2: 100 µl OptiMEM + 4 µl Lipofectamine LTX

694 The two tubes were mixed and incubated for 5 minutes separately, and then 5 minutes together.
695 The transfection mix was added drop wise to cells and incubated for 4-6 hours at 37 °C.
696 Subsequently, the transfection mix was removed and media with Pen-Strep was added.
697 Performing transfection without Pen-Strep is very important and greatly affects transfection
698 efficiency. If the cells are kept longer than 6 hours in the transfection mix, cell viability can become
699 compromised.

700 **Immunofluorescence.** All immunofluorescence experiments were performed on cells seeded on
701 glass in MatTek plates (MatTek Co., Ashland, MA, USA). Cells were fixed in 4%
702 paraformaldehyde, washed with 0.01% Triton X100 PBS and permeabilised by incubation in 0.2
703 % Triton X100, PBS for 20 minutes at room temperature. Samples were subsequently blocked

704 for 1 hour with 5%BSA, 0.01% Triton X100 PBS before incubation with Phalloidin-Atto633 (Sigma,
705 # 68825-10NMOL) and DAPI (Sigma, # d9542-5mg) in 5%BSA, 0.01% Triton X100 PBS 1 hr at
706 RT. Primary antibody was washed off in 3 washes of 5 minutes with 0.01 % Triton X100, PBS,
707 and then retained in PBS until imaging.

708 **Luciferase assay.** Luciferase assays were performed with the dual luciferase assay kit
709 (Promega). Cells were lysed using passive lysis buffer. Lysates were placed into a white 96-well
710 plate (Perkin Elmer) to assess Luciferase and Renilla activities using Envision Multilabel plate
711 reader (Perkin Elmer). To normalize, the measurements of firefly luciferase activities were
712 normalized to the renillla luciferase activities of the same sample.

713 **Western Blot.** For protein analysis, cells were lysed with 1 x SDS sample buffer (0.32 M Tris pH
714 6.8, 10% SDS, 50% glycerol, 3M β-mercaptoethanol, 0.05% bromophenol blue) added directly to
715 wells, and then cells were scraped and collected. Each sample was sonicated and then boiled at
716 95 °C for 5min before being used for Western blotting. Samples were separated on SDS-PAGE
717 gels (Bio-rad). A pre-stained Dual Colour protein ladder (Bio-rad, #1610374) was run with the
718 samples. The proteins in the gel were transferred to polyvinylidene fluoride (PVDF) membrane
719 (GE Healthcare Life Sciences). The membranes were blocked with 2% milk (Marvel) or 2%BSA
720 in TBST (137 mM NaCl, 2.7 mM KCl, 20 mM Tris HCl, pH 7.4, 0.01% Tween 20) for 1 hour at RT,
721 and then incubated with primary antibody at 4°C overnight in 0.1% milk/BSA TBST. After 3
722 washes with TBST, membranes were incubated 45 min at RT with HRP-labelled secondary
723 antibody in 0.5% milk TBST (1:50 000, Fisher Scientific). The blot was then developed by rinsing
724 it for 1 minute in Luminata WesternHRP Substrate (Millipore) before being exposed in the
725 ImageQuant600RGB machine (GE Healthcare Life Sciences). The list of antibodies used for
726 Western blotting is outlined below.

Antibody	Species	Source	WB	IF
YAP1 (D8H1X)	rabbit mono IgG	Cell Signalling Technology, #14074	1:1000	1:500
TAZ (V386)	rabbit poly	Cell Signalling Technology, #4883	1:1000	1:200
β-tubulin	mouse mono IgG1	Sigma, #T7816	1:5000	1:1000
RFP (5F8)	rat mono IgG2a	Chromotek, #5F8-100	1:1000	N/A
flag tag	mouse mono IgG1	Sigma, #F1804	1:1000	N/A

727

728 **Statistical analysis.** Statistical analyses were performed using Prism software (GraphPad
729 Software). p-values were obtained using Mann-Whitney unpaired t–test or Wilcoxon matched-
730 pairs signed rank test, with significance set at $p < 0.05$. Graphs show symbols describing p-values:
731 *, $p < 0.05$; **, $p < 0.01$; ***, $p < 0.001$, ****, $p<0.0001$; ns, not significant.

732 **FLIP imaging.** Cells were plated at low confluence and cultured overnight in glass bottom MatTek
733 dishes. Cells were transfected, and 24-48 hrs after DNA transfection imaged. One hour prior to
734 imaging, the medium was changed to Leibovitz L-15 media with 10% serum. The cells were
735 subsequently imaged with a Zeiss LSM880 microscope equipped with an argon laser (Zeiss,
736 Germany) and a 63X objective (Zeiss, alpha-Plan Apochromat 63x/1.46 NA oil korr TIRF). For
737 FLIP experiments, bleaching was performed using the laser at 100% capacity with a wavelength
738 corresponding to fluorophore excitation wavelength at a single square ROI of 8x8 pixels (4.4
739 mm2). All images were 12-bit and 256x256 pixels. Before photobleaching, 3 measurements of
740 fluorescence were taken. The ROI was then photobleached between every frame for 2 seconds
741 using maximum laser power. A series of 150 images were taken every 2 seconds for up to 5
742 minutes. For nucFLIP, bleaching region was placed in the nucleus, whilst in the cytoplasm for
743 cytoFLIP.

744 **Optogenetics light activation.** Cells were plated at low confluence and cultured overnight in
745 glass bottom MatTek dishes. Cells were transfected, and 24-48 hrs after DNA transfection
746 imaged. One hour prior to imaging, the media was changed to Leibovitz L-15 medium with 10%
747 serum supplemented with MitoTracker Deep Red (10 000x, #M22426) for staining the
748 mitochondria. Half an hour prior to imaging, the medium was changed again to Leibovitz L-15
749 medium with 10% serum without the stain.

750 The cells were subsequently imaged with a Zeiss LSM880 microscope equipped with an argon
751 laser (Zeiss, Germany) and a 40X objective (Zeiss, Plan Apochromat 40x/1.3 NA oil korr DIC
752 M27) with an environmental chamber set at 37°C. Optogenetic activation was performed using
753 458 nm laser line at 1% laser power on the bleaching function with 50 iterations selecting an area
754 encompassing the whole cell. Before activation, 5 frames were imaged without
755 photoactivation/bleaching function. Then, 150 frames of release with photoactivation and 150
756 frames of recovery without photoactivation were acquired. Frames were acquired approximately
757 4 sec apart, as this corresponds to the approximate speed of light recovery of AsLOV2 domain
758 (Strickland et al., 2012, Strickland et al., 2010). In order to simultaneously acquire two or three
759 other channels, a beam splitter 458/514/561/633 was used, which allows imaging in the cyan,
760 yellow, red and far-red colours compatible with light activation at 458 nm. Nuclei are imaged with

761 very low 458 nm laser power which did not interfere with light activation at the same wavelength.
762 Mitochondria are imaged in the far-red spectrum. The proteins of interest can be placed in the
763 yellow (Venus) or the red (mCherry) channels.

764 **3D optogenetics light activation**. All the experiments in 3D were performed on LLSM (lattice
765 light sheet microscope) in the Advanced Imaging Center at the Howard Hughes Medical Institute,
766 Janelia Research Campus. HaCaT cells were seeded on uncoated coverslips (CS-5R; Warner
767 Instruments) in a 30 ul droplet 10 000-30 000 cells/droplet and left to settle for 1hr before filling
768 the plate well with media. Cells were transfected as in 2D condition.

769 The LLSM system was configured and operated as previously described (Chen et al., 2014).
770 Samples were kept at 37°C and illuminated using a 445 nm laser (Oxxius diode laser, initial laser
771 power 132 mW) at 100% acousto-optic tunable filter transmittance, 560 nm laser (MPB fiber laser,
772 rated 500 mW) at 100% acousto-optic tunable filter transmittance and 642 nm laser (MPB fiber
773 laser, rated 500 mW) at 10% acousto-optic tunable filter transmittance. Excitation objective was
774 Special Optics 0.65 NA lens and detection objective was Nikon CFI Apo LWD 25x– Water dipping,
775 63x magnification, 1.1 NA, signal detected on two Hamamatsu Orca Flash 4.0 v2 sCMOS
776 cameras. To separate the signal between two cameras, for channel detecting MitoTracker
777 DeepRed we used Camera A BLPO-647R-25 long band pass filter. For Camera B we used NF03-
778 t42E-25 (Notch filter), BLP01-458R-25 long pass and FF01-465/537/623-25 beam splitter. Signal
779 was split with a dichroic mirror FF640-FDi014 to detect H2B-mTurquoise and mCherry. For the
780 release phase 80 frames with 445 nm laser on were acquired, and in the recovery phase 4 cycles
781 of 19 frames without and 1 frame with 445 nm laser were imaged ("staggered release"). In
782 addition providing novel information about protein dynamics, staggered release can be used to
783 map the position of the nucleus. The software used to operate the instrument and collect data
784 was LabView (National Instruments). FIJI was used for the quantification of fluorescent intensity
785 in different regions of interest. FIJI was also used to convert files into .h5 format for subsequent
786 3D visualization and the generation of movies using Imaris.

787 **Immunofluorescence quantification for nuclear-to-cytoplasmic ratios.** For quantification of
788 subcellular localization of protein of interest, the nuclear-to-cytoplasmic ratio was calculated
789 manually. For each cell, a single region of interest (ROI) square of 8x8 pixels was placed in the
790 nucleus and cytoplasm. ROIs were always selected in the DAPI channel of IF images to avoid
791 bias. The cytoplasmic ROI was then confirmed to be in the correct cell by checking the actin
792 channel. The nuclear ROI was divided by the cytoplasmic ROI to derive nuclear-to-cytoplasmic
793 ratio.

794 **FLIP quantification.** For quantification of FLIP (Fluorescent Loss In Photobleaching)
795 experiments, MetaMorph (Molecular Devices) was used to follow the integrated intensities of six
796 different square ROIs of the same size as the bleached ROI: the bleached ROI, two reporting
797 ROIs (one in the same compartment as the bleached point and one in the other compartment),
798 two controls ROIs (one in the nucleus and one in the cytoplasm of one control cell) and one ROI
799 outside any cells to measure the background intensity. The two nuclear ROIs and the cytoplasmic
800 ROI of the bleached cells were positioned to be at approximately equal distances from one
801 another. To normalize, first the background intensity was subtracted from the five other intensities
802 measured in the cells. Then, the intensities measured in the cell of interest (three ROIs) were
803 normalized by dividing by the average intensity of the two control ROIs. These data were plotted
804 in the illustrative graphs.

805 To extract import and export rates, the nuclear and cytoplasmic compartments were determined
806 manually in MATLAB using the roipoly command (Image Processing toolbox). The total population
807 intensity of each compartment over time was then extracted based on these defined regions.
808 Background subtraction and normalisation to the average of nuclear and cytoplasmic regions in
809 a control cell was then carried out (as above). A simpler differential equation model than that
810 employed in (Ege et al., 2018) was then fitted to this dynamic intensity data, including only
811 temporal data and not spatial data. We fit to the population intensities using a system of ODEs
812 given by

813 $$\frac{dn(t)}{dt} = -k_{exp}n(t) + k_{imp}c(t) - \delta_n\left(\eta_1 n(t) + \lambda e^{(-\eta_2 t)}\right),$$

814 $$\frac{dc(t)}{dt} = k_{exp}n(t) - k_{imp}c(t) - \delta_c\left(\eta_1 c(t) + \lambda e^{(-\eta_2 t)}\right),$$

815 $$\delta_n = \begin{cases} 1, & \text{bleach in nucleus} \\ 0, & \text{else} \end{cases}, \delta_c = \begin{cases} 1, & \text{bleach in cytoplasm} \\ 0, & \text{else} \end{cases},$$

816 where $n(t)$ and $c(t)$ give, respectively, the total nuclear and cytoplasmic intensities at time, t. The
817 parameter k_{exp} gives the export rate from the nucleus to the cytoplasm and k_{imp} the import rate
818 from the cytoplasm to the nucleus. The final functions correspond to intensity decay due to
819 bleaching depending on whether the bleach is in the nucleus or cytoplasm. A single decay
820 parameter η_1 allows the model to fit the bleach reasonably well, but underestimates the rapid
821 initial bleach. Hence a decaying exponential function is also incorporated such that the bleach is
822 effectively modelled by a double exponential, one with a rapid rate and the other a slower rate.
823 This double exponential will clearly estimate the rate of bleaching better than a single exponential

824 could (due to a greater degree of fitting freedom) and allows more robust estimates of population
825 intensity transfer between compartments. The initial conditions are given by $n(0) = n_0$ and $c(0) =$
826 c_0. At steady-state, prior to bleaching,

827 $$n_0 = k_{imp}/k_{exp}c_0. \quad (1)$$

828 An analytic solution to the ODEs exists, however we estimated parameters by fitting a numerical
829 solution of the model to the experimental intensity data for each cell. Parameter estimates for
830 k_{exp}, k_{imp}, n_0, c_0, η_1, η_2 and λ were all required. We can reduce the number of parameters to fit
831 by one by taking advantage of the steady-state relationship (1) to fix the initial nuclear intensity in
832 terms of rates and initial cytoplasmic intensity. To optimise parameter fitting, we used the
833 nonlinear model fitting function nlinfit in MATLAB's Statistics and Machine Learning toolbox. Initial
834 guesses for parameters in the nlinfit function were selected by choosing the initial cytoplasmic
835 intensity in the experimental data for c_0 and initial guess of order 10^{-3} based on population intensity
836 analysis carried out in (Ege et al., 2018) for k_{exp} and k_{imp}. To generate initial guesses for the
837 bleaching decay rates we fitted a double exponential function

838 $$a(t) = q_1 e^{(-r_1 t)} + q_2 e^{(-r_2 t)}$$

839 to the total intensity of the entire cell (nucleus and cytoplasm). Initial guesses to this double
840 exponential fit were given as: $[\tilde{q}_1, \tilde{q}_2, \tilde{r}_1, \tilde{r}_2]$=[a(0)/2,a(0)/2,0.5,0.1]. By differentiating this double
841 exponential, $a(t)$, into the form

842 $$\frac{da(t)}{dt} = -\eta_1 a(t) - \lambda e^{(-\eta_2 t)}$$

843 the output parameters fitted to the double exponential could be used as initial guesses for η_1,
844 η_2 and λ.

845 **Optogenetic quantification.**

846 **Opto_analyser – A Cell Compartment Segmentation App.**

847 To segment cellular compartments and extract dynamic intensities of the mitochondria, cytoplasm
848 and nucleus we developed an app in MATLAB. The labelling of the nucleus and mitochondria
849 alongside the GFP labelling of the protein of interest allow temporal segmentation of each
850 compartment. This is done by the user selecting appropriate threshold levels in addition to
851 carrying out a number of other processing steps. Appropriate compartment threshold levels differ
852 from frame to frame and it would be too time consuming to threshold every compartment for every

853 frame for every cell. In addition, in some frames the signal from a given compartment could be
854 too weak to segment independently. Therefore, the movie is split into time windows of multiple
855 frames. For example, for a movie of 100 frames, a window split of 4 would split the movie into
856 four windows of 25 frames each whilst a single window split would provide only a single window
857 covering all 100 frames. Intensity projections of each of these multiple framed windows are used
858 in order to segment the compartments. A window split of 4 would then provide four segmented
859 binary images that covered all 25 frames in each of their respective windows. This doesn't provide
860 total sensitivity to dynamic morphological changes but captures some of it whilst still being robust
861 to high levels of noise and low levels of signal. A single window-split is obviously most robust to
862 high noise and low signal but offers no sensitivity to morphological changes. Increasing the
863 number of time windows leads to greater sensitivity to dynamic compartment movement within
864 the movie but reduces robustness in segmentation due to the projections being taken from fewer
865 frames in each window. In the analysis carried out here, a single percentile intensity projection of
866 the entire movie (single window split) and percentile intensity projections of the movie split into 2,
867 4 and 8 time windows (multiple window splits) were considered.

868 The app was developed in MATLAB, using its inbuilt App Designer software and requires the
869 Image Processing toolbox and lsmread from https://github.com/joe-of-all-trades/lsmread. The
870 user interface is composed of three main panels. The left-hand side panel is for user input of file
871 locations, requested number of window splits and save location. It also outputs error messages
872 to guide the user. The central panel is composed of multiple tabs where the majority of image
873 processing takes place. Each of these separate aspects of the image segmentation is carried out
874 in a separate tab. Segmentation steps of the nuclear and mitochondrial compartments rely on the
875 nuclear and mitochondrial channels only. Segmentation of the whole cell boundary relies on the
876 generation of a hybrid channel where each frame is the maximum intensity projection of the
877 nuclear, mitochondrial and protein channels in that frame. This makes the segmentation more
878 robust to the heterogeneous and potentially weak intensity of the protein channel. Previews of the
879 first frames in each channel allow the user to define each channel before zooming in on the region
880 of interest around the cell. The app then iterates through each of the chosen time window splits
881 in ascending order of number of windows (e.g. a single split is analysed first, followed by a two
882 window split). For each selected window split, the app allows the user to define the intensity
883 projections of the nuclear, mitochondrial and hybrid channels for all windows in that split
884 simultaneously. The projections are generated via user defined percentiles of intensity of all
885 frames in the relevant channel in that window. High percentiles allow objects to be visible for weak
886 signals. Low percentiles can reduce noise and interference from neighbouring cells when the

signals are strong. The optimum selected percentile is one that maximises the features of the cell under consideration but minimises interference from neighbouring cells and noise. Segmentation is carried out on these percentile intensity projections. Having selected the percentiles for all windows in that window split, the app then iterates through each of the window split's windows. For each time window, the user manually crops around the cell to isolate the cell under consideration from neighbours, selecting from a choice of projections that best aid visual cropping. Using input sliders, they then select the desired threshold for segmentation of the hybrid channel, in order to determine the cell boundary in that time window. Images illustrating the current cell boundary are updated in real time as the threshold is adjusted. Having segmented the cell boundary, the user selects the most appropriate threshold levels for segmenting the nuclear and mitochondrial compartments. Again, images illustrating the compartment boundaries are updated in real time as the threshold levels are adjusted. Population intensities for each compartment over time are taken by using the segmented compartments as masks and applying them to the protein channel. The same compartment mask is used for all frames specific to each window. The right-hand side panel includes plots of each compartment population versus time, that update instantly according to chosen threshold levels, in addition to a record of all percentile and threshold choices for each time window in each window split. All previous population intensity profiles for previously completed window splits are included with easy to interpret colour mapping identifying each window split. For the current window split, the population intensity profiles include all windows up to and including the window currently being segmented. These plots and this data allows the user to determine the most appropriate thresholds not only from the thresholded images, but also from the emerging shape of the population intensity profiles and previously selected percentile and threshold levels. The presentation of all previous window-splits allows the user to investigate how the number of windows affects the resulting population intensity profiles. The plotting of all completed windows in the current window split allows the user to observe how smoothly the population intensity profile of the current window links with the previous one as the threshold levels of the current window are altered. Finally, once all window splits have been completed the segmentations are interpolated between time windows. A moving median filter is applied to intensity values of each frame of each compartment channel (nucleus, mitochondria and hybrid) with the size of the median filter being determined by the length of the windows for each split (i.e. if a movie of 100 frames is split into four windows of 25 frames each then the moving median filter has a range of 25 frames). Compartment thresholds are interpolated from the time window thresholds across all frames. Finally, the rough cell boundary crop (to limit interference from neighbouring objects) for each time window is interpolated across all frames by using distance

921 transforms to model the change in shape from one binary crop to the next over the appropriate
922 number of frames in the time window. This generates segmented compartments that change on
923 a frame-by-frame basis rather than a window-by-window basis. Population intensities over time
924 are then generated for these interpolated segmented compartments.

925 **Background subtraction, bleaching intensity normalisation and non-conserved intensity**
926 **correction methods**

927 Intensity normalisation consists of three stages: i) background subtraction, ii) normalisation due
928 to bleaching and iii) correcting for escape and return of the protein from the focal plane. The
929 normalisation to account for bleaching should lead to the total intensity being constant over time
930 and this is also what is assumed by the system of ODEs. However, upon release from the
931 mitochondria, the protein of interest does not always remain in the viewing plane and instead
932 escapes elsewhere in the cell. Similarly, during the recovery phase there can be a dramatic inflow
933 of the protein of interest in the viewing plane.

934 Background subtraction is carried out for each frame. The mean of a 20 pixel by 20 pixel square
935 in the top left hand corner of the movie is calculated over time and subtracted from the
936 compartment intensities.

937 The intensities are then normalised to account for laser bleaching. The level of laser bleaching is
938 determined from the behaviour of the total intensity of the cell over time, which appears to be
939 nonlinear. The rate of bleaching appears to be composed of two approximately linear phases
940 with gradients being approximately linear in both the release and recovery phases but with
941 differing rates. As such, the total intensity is split into release and recovery phases and a linear fit
942 made to each section. For all time prior to recovery, the bleach is assumed to fit the linear fit to
943 total intensity in the release phase. From the first point of recovery, bleaching is assumed to fit
944 the linear fit to bleaching of total intensity in the recovery phase.

945 Since the total intensity is not necessarily conserved due to inflow and outflow from the plane of
946 view, the linear fits in each release and recovery phase are fit to temporal subsections. This avoids
947 fitting a linear model to total intensity profiles that also include rapid outflow or inflow into the
948 viewing plane in addition to low level bleaching. Let C be the median total intensity of the cell over
949 the interval $[0, t_{ss_{end}}]$ where $t_{ss_{end}}$ is the last time-point prior to optorelease. Let t_{rl_1} be the
950 beginning of the release fitting subsection and t_{rl_2} be the end. The linear fit to total intensity
951 between t_{rl_1} and t_{rl_2} is given by $\tilde{y}_{rel} = p_{rel_1} t + \tilde{p}_{rel_2}$ where we impose $p_{rel_1} \leq 0$. Let t_{rc_1} be the

beginning of the recovery fitting subsection and t_{rc_2} be the end. The linear total intensity fit between t_{rc_1} and t_{rc_2} is given by $\tilde{y}_{rec} = p_{rec_1} t + \tilde{p}_{rec_2}$ where we impose $p_{rec_1} \leq 0$. To normalise to bleaching over these two phases requires a smooth bilinear fit to the gradual drop in total intensity. In the absence of inflow and outflow from the focal plane, these two linear fits, $\tilde{y}_{rel}$ and $\tilde{y}_{rec}$ should smoothly connect at the end of the release and beginning of the recovery phase ($t = t_{REC_1}$). The linear fit $\tilde{y}_{rel}$ should also smoothly link with the median steady-state intensity, C, at timepoint $t_{ss_{end}}$ and linearly increase beyond this value for $t < t_{ss_{end}}$. However, in cases where the total intensity is not conserved throughout the experiment, we must translate the linear functions $\tilde{y}_{rel}$ and $\tilde{y}_{rec}$ such that $\tilde{y}_{rel}$ smoothly connects with C and $\tilde{y}_{rec}$. We adjust the y-intercept for the release phase according to

$$p_{rel_2} = \begin{cases} \tilde{p}_{rel_2}, & p_{rel_1} t_{ss_{end}} + \tilde{p}_{rel_2} > C \\ C - p_{rel_1} t_{ss_{end}}, & \text{else} \end{cases}$$

and define our translated linear fit as $y_{rel} = p_{rel_1} t + p_{rel_2}$. This links the release fit to the median steady-state intensity. We then adjust the y-intercept of $\tilde{y}_{rec}$ so it lines up with y_{rel} by setting $p_{rec_2} = \left(p_{rel_1} - p_{rec_1}\right) t_{REC_1} + p_{rel_2}$. We then define our translated linear fit to the recovery phase as $y_{rec} = p_{rec_1} t + p_{rec_2}$. This gives us a smooth bilinear fit to drop in intensity due to bleaching that is independent of inflow and outflow and fit to differing bleach rates in the release and recovery phases.

Following background subtraction and normalisation of intensity to account for bleaching, we address the issue of non-conserved intensity due to rapid inflow and outflow from the image plane. In some cells, intensity is relatively well conserved. However, in a large number of cases we observe a rapid outflow from the image plane during release and rapid inflow during recovery. In a very small number of cases, we observe rapid inflow to the image plane during release and rapid outflow from the image plane during recovery. Due to the low number of cases of the latter, we only correct for the outflow-inflow case.

To detect cases of rapid outflow in release and rapid inflow in recovery we make use of the initial non-translated linear fits $\tilde{y}_{rel}$ and $\tilde{y}_{rec}$ and the median steady-state intensity, C. Firstly, if $\tilde{y}_{rel}\left(t_{ss_{end}}\right) < C$ it suggests a discontinuous drop in total intensity upon release. This implies a rapid outflow from the focal plane upon release. Secondly, if $\tilde{y}_{rel}\left(t_{REC_1}\right) < \tilde{y}_{rec}\left(t_{REC_1}\right)$ it suggests discontinuous increase in total intensity upon recovery. This implies a rapid inflow into the focal plane upon recovery. If both of these conditions are satisfied it suggests rapid outflow followed by

rapid inflow that we can correct for in the model. If these conditions are satisfied, the narrow time periods of rapid outflow and inflow are identified and the total intensity over these time periods smoothed independently using Lowess. By considering the intensity profiles and the first derivative profiles, a smooth, monotonically decreasing outflow and smooth monotonically increasing inflow can be generated in the system. A vector of inflow and outflow with the smoothed intensity values over these two time windows and NaNs (not a number) everywhere else is generated.

Mathematical model

As in the FLIP analysis, we fit a system of ODEs to the extracted population intensity data for the mitochondrial, cytoplasmic and nuclear compartments. The ODEs are given by

$$\frac{dm(t)}{dt} = k_{rec}c(t) - K_{rel}m(t) + \phi(t)$$

$$\frac{dc(t)}{dt} = -k_{rec}c(t) + K_{rel}m(t) + k_{exp}n(t) - k_{imp}c(t),$$

$$\frac{dn(t)}{dt} = -k_{exp}n(t) + k_{imp}c(t),$$

where $m(t)$, $c(t)$ and $n(t)$ are the mitochondrial, cytoplasmic and nuclear intensities respectively at time, t. The initial conditions are given by $m(0) = m_0$, $c(0) = c_0$ and $n(0) = n_0$. The rate of export from the nucleus to the cytoplasm and rate of import from the cytoplasm to the nucleus are given by k_{exp} and k_{imp} respectively. The parameter k_{rec} gives the rate at which the protein leaves the cytoplasm and binds to the mitochondria. The parameter K_{rel} gives the rate at which protein leaves the mitochondria and enters the cytoplasmic compartment. The value K_{rel} is dependent on whether the system is in the illumination phase or not i.e.

$$K_{rel} = \begin{cases} k_{rel_{ill}}, & \text{system in illumination phase} \\ k_{rel_{ss}}, & \text{system in steady} - \text{state phase.} \end{cases}$$

The final component of the ODEs is the function, $\phi(t)$, which accounts for cases where the total protein intensity in the system is not conserved in the experimental data, even after normalisation. We shall refer to this further in the model fitting methodology.

Model Fitting

The system of ODEs is fitted to the experimental data using MATLAB's nlinfit function from the Statistics and Machine Learning toolbox. The fitting weights of each compartment are normalised

such that each compartment contributes an equal amount to the residuals. Parameters that need fitting in the system are the rates k_{exp}, k_{imp}, k_{rec}, $k_{rel_{ill}}$ and $k_{rel_{ss}}$ and the initial conditions m_0, c_0 and n_0. The model is fit such that the parameter $k_{rel_{ill}}$ is fit only at the release phase and $k_{rel_{ss}}$ only fit at the initial steady-state phase and the recovery phase. The initial conditions need to be fitted since we cannot fix them at their experimental measurements due to noise in the system. We can reduce the number of parameters that need fitting by taking advantage of the steady-state relationships $c_0 = k_{rel_{ss}}/k_{rec}m_0$ and $n_0 = k_{imp}/k_{exp}c_0$ allowing us to fix the initial nuclear and cytoplasmic intensities in terms of other parameters. If the algorithm has identified that total intensity is conserved throughout the experiment then the inflow-outflow function $\phi(t)$ is set to zero everywhere. If the intensity is not conserved then $\phi(t)$ is constructed from the derivative of the inflow-outflow vector (described in the normalisation section) in the sections of smooth, monotonically decreasing release and smooth, monotonically increasing recovery. Everywhere else, where the inflow-outflow vector is composed of NaNs, the function $\phi(t)$ is set to zero. As initial guesses for our parameters we take $[\hat{k}_{rel_{ss}}, \hat{k}_{rel_{ill}}, \hat{k}_{rec}, \hat{k}_{imp}, \hat{k}_{exp}, \hat{m}_0] = [0.05, 0.10, 0.05, 0.005, 0.005, \Lambda]$ where Λ gives the median mitochondrial intensity over the first five frames prior to release.

For each cell, the intensity extraction was carried out by splitting each movie into 1, 2, 4 or 8 sections as described in the segmentation section. The system of ODEs was fit to each of these intensity extractions and the mean sum of squares of error for both the entire system and the fit to the nucleus only calculated. The fit with the lowest mean sum of squares of error was selected as being the optimum fit in each case.

Acknowledgements

We thank members of the Crick Advanced Light Microscopy facility for technical support. We are indebted to and Hui Wang and Sirio Dupont for thoughtful discussion and advice.

Competing interests

The authors declare no competing interests.

Funding

A.D., R.P.J, M.M., and E.S. were funded by the Francis Crick Institute, which receives its core funding from Cancer Research UK (FC010144), the UK Medical Research Council (FC010144) and the Wellcome Trust (FC010144). M.M. also received funding from Marie Curie Actions—Intra-European Fellowships #625496 and BIRD Seed grant from Department of Molecular Medicine (University of Padua). K.H. was supported by NIH grant R35GM122596. The Advanced Imaging Center at is a jointly funded venture between HHMI and the Gordon and Betty Moore Foundation.

Author contributions

A.M.D. performed the experiments, R.P.J. developed the app and analytical methods, K.H. provided reagents prior to their publication, J.M.H. facilitated lattice light sheet imaging, T.F. and A.C. assisted with 3D data processing, M.M. and E.S. conceived the study, A.M.D., M.M., and E.S. wrote the manuscript.

References

ARAGONA, M., PANCIERA, T., MANFRIN, A., GIULITTI, S., MICHIELIN, F., ELVASSORE, N., DUPONT, S. & PICCOLO, S. 2013. A mechanical checkpoint controls multicellular growth through YAP/TAZ regulation by actin-processing factors. *Cell,* 154**,** 1047-1059.

AZZOLIN, L., PANCIERA, T., SOLIGO, S., ENZO, E., BICCIATO, S., DUPONT, S., BRESOLIN, S., FRASSON, C., BASSO, G., GUZZARDO, V., FASSINA, A., CORDENONSI, M. & PICCOLO, S. 2014. YAP/TAZ incorporation in the beta-catenin destruction complex orchestrates the Wnt response. *Cell,* 158**,** 157-70.

BASU, S., TOTTY, N. F., IRWIN, M. S., SUDOL, M. & DOWNWARD, J. 2003. Akt phosphorylates the Yes-associated protein, YAP, to induce interaction with 14-3-3 and attenuation of p73-mediated apoptosis. *Mol Cell,* 11**,** 11-23.

BEHAR, M. & HOFFMANN, A. 2010. Understanding the temporal codes of intra-cellular signals. *Curr Opin Genet Dev,* 20**,** 684-93.

BENHAM-PYLE, B. W., PRUITT, B. L. & NELSON, W. J. 2015. Cell adhesion. Mechanical strain induces E-cadherin-dependent Yap1 and beta-catenin activation to drive cell cycle entry. *Science,* 348**,** 1024-7.

BERTOLIO, R., NAPOLETANO, F., MANO, M., MAURER-STROH, S., FANTUZ, M., ZANNINI, A., BICCIATO, S., SORRENTINO, G. & DEL SAL, G. 2019. Sterol regulatory element binding protein 1 couples mechanical cues and lipid metabolism. *Nat Commun,* 10**,** 1326.

BEYER, H. M., JUILLOT, S., HERBST, K., SAMODELOV, S. L., MULLER, K., SCHAMEL, W. W., ROMER, W., SCHAFER, E., NAGY, F., STRAHLE, U., WEBER, W. & ZURBRIGGEN, M. D. 2015. Red Light-Regulated Reversible Nuclear Localization of Proteins in Mammalian Cells and Zebrafish. *ACS Synth Biol,* 4**,** 951-8.

CAI, D., FELICIANO, D., DONG, P., FLORES, E., GRUEBELE, M., PORAT-SHLIOM, N., SUKENIK, S., LIU, Z. & LIPPINCOTT-SCHWARTZ, J. 2019. Phase separation of YAP reorganizes genome topology for long-term YAP target gene expression. *Nat Cell Biol,* 21**,** 1578-1589.

CALVO, F., EGE, N., GRANDE-GARCIA, A., HOOPER, S., JENKINS, R. P., CHAUDHRY, S. I., HARRINGTON, K., WILLIAMSON, P., MOEENDARBARY, E., CHARRAS, G. & SAHAI, E. 2013. Mechanotransduction and YAP-dependent matrix remodelling is required for the generation and maintenance of cancer-associated fibroblasts. *Nat Cell Biol,* 15**,** 637-46.

CHAN, S. W., LIM, C. J., LOO, L. S., CHONG, Y. F., HUANG, C. & HONG, W. 2009. TEADs mediate nuclear retention of TAZ to promote oncogenic transformation. *J Biol Chem,* 284**,** 14347-58.

CHAUDHURI, O., GU, L., KLUMPERS, D., DARNELL, M., BENCHERIF, S. A., WEAVER, J. C., HUEBSCH, N., LEE, H. P., LIPPENS, E., DUDA, G. N. & MOONEY, D. J. 2016. Hydrogels with tunable stress relaxation regulate stem cell fate and activity. *Nat Mater,* 15**,** 326-34.

CHEN, B. C., LEGANT, W. R., WANG, K., SHAO, L., MILKIE, D. E., DAVIDSON, M. W., JANETOPOULOS, C., WU, X. S., HAMMER, J. A., 3RD, LIU, Z., ENGLISH, B. P., MIMORI-KIYOSUE, Y., ROMERO, D. P., RITTER, A. T., LIPPINCOTT-SCHWARTZ, J., FRITZ-LAYLIN, L., MULLINS, R. D., MITCHELL, D. M., BEMBENEK, J. N., REYMANN, A. C., BOHME, R., GRILL, S. W., WANG, J. T., SEYDOUX, G., TULU, U. S., KIEHART, D. P. & BETZIG, E. 2014. Lattice light-sheet microscopy: imaging molecules to embryos at high spatiotemporal resolution. *Science,* 346**,** 1257998.

CODELIA, V. A., SUN, G. & IRVINE, K. D. 2014. Regulation of YAP by mechanical strain through Jnk and Hippo signaling. *Curr Biol,* 24**,** 2012-7.

CREFCOEUR, R. P., YIN, R., ULM, R. & HALAZONETIS, T. D. 2013. Ultraviolet-B-mediated induction of protein-protein interactions in mammalian cells. *Nat Commun,* 4**,** 1779.

1100 DE MENA, L., RIZK, P. & RINCON-LIMAS, D. E. 2018. Bringing Light to Transcription: The
1101 Optogenetics Repertoire. *Front Genet,* 9**,** 518.
1102 DI VENTURA, B. & KUHLMAN, B. 2016. Go in! Go out! Inducible control of nuclear localization.
1103 *Curr Opin Chem Biol,* 34**,** 62-71.
1104 DUPONT, S., MORSUT, L., ARAGONA, M., ENZO, E., GIULITTI, S., CORDENONSI, M.,
1105 ZANCONATO, F., LE DIGABEL, J., FORCATO, M., BICCIATO, S., ELVASSORE, N. &
1106 PICCOLO, S. 2011. Role of YAP/TAZ in mechanotransduction. *Nature,* 474**,** 179-83.
1107 EGE, N., DOWBAJ, A. M., JIANG, M., HOWELL, M., HOOPER, S., FOSTER, C., JENKINS, R.
1108 P. & SAHAI, E. 2018. Quantitative Analysis Reveals that Actin and Src-Family Kinases
1109 Regulate Nuclear YAP1 and Its Export. *Cell Syst,* 6**,** 692-708 e13.
1110 ELBEDIWY, A., VINCENT-MISTIAEN, Z. I., SPENCER-DENE, B., STONE, R. K., BOEING, S.,
1111 WCULEK, S. K., CORDERO, J., TAN, E. H., RIDGWAY, R., BRUNTON, V. G., SAHAI,
1112 E., GERHARDT, H., BEHRENS, A., MALANCHI, I., SANSOM, O. J. & THOMPSON, B. J.
1113 2016. Integrin signalling regulates YAP and TAZ to control skin homeostasis.
1114 *Development,* 143**,** 1674-87.
1115 ELOSEGUI-ARTOLA, A., ANDREU, I., BEEDLE, A. E. M., LEZAMIZ, A., UROZ, M.,
1116 KOSMALSKA, A. J., ORIA, R., KECHAGIA, J. Z., RICO-LASTRES, P., LE ROUX, A. L.,
1117 SHANAHAN, C. M., TREPAT, X., NAVAJAS, D., GARCIA-MANYES, S. & ROCA-
1118 CUSACHS, P. 2017. Force Triggers YAP Nuclear Entry by Regulating Transport across
1119 Nuclear Pores. *Cell,* 171**,** 1397-1410 e14.
1120 ENGELKE, H., CHOU, C., UPRETY, R., JESS, P. & DEITERS, A. 2014. Control of protein
1121 function through optochemical translocation. *ACS Synth Biol,* 3**,** 731-6.
1122 FANG, L., TENG, H., WANG, Y., LIAO, G., WENG, L., LI, Y., WANG, X., JIN, J., JIAO, C., CHEN,
1123 L., PENG, X., CHEN, J., YANG, Y., FANG, H., HAN, D., LI, C., JIN, X., ZHANG, S., LIU,
1124 Z., LIU, M., WEI, Q., LIAO, L., GE, X., ZHAO, B., ZHOU, D., QIN, H. L., ZHOU, J. &
1125 WANG, P. 2018. SET1A-Mediated Mono-Methylation at K342 Regulates YAP Activation
1126 by Blocking Its Nuclear Export and Promotes Tumorigenesis. *Cancer Cell,* 34**,** 103-118
1127 e9.
1128 FU, X., LIANG, C., LI, F., WANG, L., WU, X., LU, A., XIAO, G. & ZHANG, G. 2018. The Rules
1129 and Functions of Nucleocytoplasmic Shuttling Proteins. *Int J Mol Sci,* 19.
1130 GAO, Z., CHEN, S., QIN, S. & TANG, C. 2018. Network Motifs Capable of Decoding Transcription
1131 Factor Dynamics. *Sci Rep,* 8**,** 3594.
1132 GUNTAS, G., HALLETT, R. A., ZIMMERMAN, S. P., WILLIAMS, T., YUMEREFENDI, H., BEAR,
1133 J. E. & KUHLMAN, B. 2015. Engineering an improved light-induced dimer (iLID) for
1134 controlling the localization and activity of signaling proteins. *Proc Natl Acad Sci U S A,*
1135 112**,** 112-7.
1136 HAO, N. & O'SHEA, E. K. 2011. Signal-dependent dynamics of transcription factor translocation
1137 controls gene expression. *Nat Struct Mol Biol,* 19**,** 31-9.
1138 KANAI, F., MARIGNANI, P. A., SARBASSOVA, D., YAGI, R., HALL, R. A., DONOWITZ, M.,
1139 HISAMINATO, A., FUJIWARA, T., ITO, Y., CANTLEY, L. C. & YAFFE, M. B. 2000. TAZ:
1140 a novel transcriptional co-activator regulated by interactions with 14-3-3 and PDZ domain
1141 proteins. *EMBO J,* 19**,** 6778-91.
1142 KENNEDY, M. J., HUGHES, R. M., PETEYA, L. A., SCHWARTZ, J. W., EHLERS, M. D. &
1143 TUCKER, C. L. 2010. Rapid blue-light-mediated induction of protein interactions in living
1144 cells. *Nat Methods,* 7**,** 973-5.
1145 KOFLER, M., SPEIGHT, P., LITTLE, D., DI CIANO-OLIVEIRA, C., SZASZI, K. & KAPUS, A. 2018.
1146 Mediated nuclear import and export of TAZ and the underlying molecular requirements.
1147 *Nat Commun,* 9**,** 4966.
1148 LU, Y., WU, T., GUTMAN, O., LU, H., ZHOU, Q., HENIS, Y. I. & LUO, K. 2020. Phase separation
1149 of TAZ compartmentalizes the transcription machinery to promote gene expression. *Nat*
1150 *Cell Biol,* 22**,** 453-464.

1151 MANNING, S. A., DENT, L. G., KONDO, S., ZHAO, Z. W., PLACHTA, N. & HARVEY, K. F. 2018.
1152 Dynamic Fluctuations in Subcellular Localization of the Hippo Pathway Effector Yorkie In
1153 Vivo. *Curr Biol,* 28**,** 1651-1660 e4.
1154 MENG, Z., MOROISHI, T. & GUAN, K. L. 2016. Mechanisms of Hippo pathway regulation. *Genes*
1155 *Dev,* 30**,** 1-17.
1156 MOLENAAR, C. & WEEKS, K. L. 2018. Nucleocytoplasmic shuttling: The ins and outs of
1157 quantitative imaging. *Clin Exp Pharmacol Physiol,* 45**,** 1087-1094.
1158 NAKAJIMA, H., YAMAMOTO, K., AGARWALA, S., TERAI, K., FUKUI, H., FUKUHARA, S.,
1159 ANDO, K., MIYAZAKI, T., YOKOTA, Y., SCHMELZER, E., BELTING, H. G., AFFOLTER,
1160 M., LECAUDEY, V. & MOCHIZUKI, N. 2017. Flow-Dependent Endothelial YAP Regulation
1161 Contributes to Vessel Maintenance. *Dev Cell,* 40**,** 523-536 e6.
1162 NIOPEK, D., BENZINGER, D., ROENSCH, J., DRAEBING, T., WEHLER, P., EILS, R. & DI
1163 VENTURA, B. 2014. Engineering light-inducible nuclear localization signals for precise
1164 spatiotemporal control of protein dynamics in living cells. *Nat Commun,* 5**,** 4404.
1165 NIOPEK, D., WEHLER, P., ROENSCH, J., EILS, R. & DI VENTURA, B. 2016. Optogenetic control
1166 of nuclear protein export. *Nat Commun,* 7**,** 10624.
1167 OKA, T. & SUDOL, M. 2009. Nuclear localization and pro-apoptotic signaling of YAP2 require
1168 intact PDZ-binding motif. *Genes Cells,* 14**,** 607-15.
1169 POCATERRA, A., ROMANI, P. & DUPONT, S. 2020. YAP/TAZ functions and their regulation at
1170 a glance. *J Cell Sci,* 133.
1171 PURVIS, J. E. & LAHAV, G. 2013. Encoding and decoding cellular information through signaling
1172 dynamics. *Cell,* 152**,** 945-56.
1173 ROSENBLUH, J., NIJHAWAN, D., COX, A. G., LI, X., NEAL, J. T., SCHAFER, E. J., ZACK, T. I.,
1174 WANG, X., TSHERNIAK, A., SCHINZEL, A. C., SHAO, D. D., SCHUMACHER, S. E.,
1175 WEIR, B. A., VAZQUEZ, F., COWLEY, G. S., ROOT, D. E., MESIROV, J. P.,
1176 BEROUKHIM, R., KUO, C. J., GOESSLING, W. & HAHN, W. C. 2012. beta-Catenin-
1177 driven cancers require a YAP1 transcriptional complex for survival and tumorigenesis.
1178 *Cell,* 151**,** 1457-73.
1179 SHREBERK-SHAKED, M. & OREN, M. 2019. New insights into YAP/TAZ nucleo-cytoplasmic
1180 shuttling: new cancer therapeutic opportunities? *Mol Oncol,* 13**,** 1335-1341.
1181 SORRENTINO, G., RUGGERI, N., SPECCHIA, V., CORDENONSI, M., MANO, M., DUPONT, S.,
1182 MANFRIN, A., INGALLINA, E., SOMMAGGIO, R., PIAZZA, S., ROSATO, A., PICCOLO,
1183 S. & DEL SAL, G. 2014. Metabolic control of YAP and TAZ by the mevalonate pathway.
1184 *Nat Cell Biol,* 16**,** 357-66.
1185 STRICKLAND, D., LIN, Y., WAGNER, E., HOPE, C. M., ZAYNER, J., ANTONIOU, C., SOSNICK,
1186 T. R., WEISS, E. L. & GLOTZER, M. 2012. TULIPs: tunable, light-controlled interacting
1187 protein tags for cell biology. *Nat Methods,* 9**,** 379-84.
1188 STRICKLAND, D., YAO, X., GAWLAK, G., ROSEN, M. K., GARDNER, K. H. & SOSNICK, T. R.
1189 2010. Rationally improving LOV domain-based photoswitches. *Nat Methods,* 7**,** 623-6.
1190 SUDOL, M. 2013. YAP1 oncogene and its eight isoforms. *Oncogene,* 32**,** 3922.
1191 TAMM, C., BOWER, N. & ANNEREN, C. 2011. Regulation of mouse embryonic stem cell self-
1192 renewal by a Yes-YAP-TEAD2 signaling pathway downstream of LIF. *J Cell Sci,* 124**,**
1193 1136-44.
1194 VALON, L., MARIN-LLAURADO, A., WYATT, T., CHARRAS, G. & TREPAT, X. 2017.
1195 Optogenetic control of cellular forces and mechanotransduction. *Nat Commun,* 8**,** 14396.
1196 VARELAS, X., MILLER, B. W., SOPKO, R., SONG, S., GREGORIEFF, A., FELLOUSE, F. A.,
1197 SAKUMA, R., PAWSON, T., HUNZIKER, W., MCNEILL, H., WRANA, J. L. & ATTISANO,
1198 L. 2010. The Hippo pathway regulates Wnt/beta-catenin signaling. *Dev Cell,* 18**,** 579-91.
1199 WADA, K., ITOGA, K., OKANO, T., YONEMURA, S. & SASAKI, H. 2011. Hippo pathway
1200 regulation by cell morphology and stress fibers. *Development,* 138**,** 3907-14.

1201 WANG, H. & HAHN, K. M. 2016. LOVTRAP: A Versatile Method to Control Protein Function with
1202 Light. *Curr Protoc Cell Biol,* 73**,** 21 10 1-21 10 14.
1203 WANG, H., VILELA, M., WINKLER, A., TARNAWSKI, M., SCHLICHTING, I., YUMEREFENDI,
1204 H., KUHLMAN, B., LIU, R., DANUSER, G. & HAHN, K. M. 2016a. LOVTRAP: an
1205 optogenetic system for photoinduced protein dissociation. *Nat Methods,* 13**,** 755-8.
1206 WANG, S., LU, Y., YIN, M. X., WANG, C., WU, W., LI, J., WU, W., GE, L., HU, L., ZHAO, Y. &
1207 ZHANG, L. 2016b. Importin alpha1 Mediates Yorkie Nuclear Import via an N-terminal Non-
1208 canonical Nuclear Localization Signal. *J Biol Chem,* 291**,** 7926-37.
1209 XU, L. & MASSAGUE, J. 2004. Nucleocytoplasmic shuttling of signal transducers. *Nat Rev Mol*
1210 *Cell Biol,* 5**,** 209-19.
1211 YOSEF, N. & REGEV, A. 2011. Impulse control: temporal dynamics in gene transcription. *Cell,*
1212 144**,** 886-96.
1213 YUMEREFENDI, H., DICKINSON, D. J., WANG, H., ZIMMERMAN, S. P., BEAR, J. E.,
1214 GOLDSTEIN, B., HAHN, K. & KUHLMAN, B. 2015. Control of Protein Activity and Cell
1215 Fate Specification via Light-Mediated Nuclear Translocation. *PLoS One,* 10**,** e0128443.
1216 YUMEREFENDI, H., LERNER, A. M., ZIMMERMAN, S. P., HAHN, K., BEAR, J. E., STRAHL, B.
1217 D. & KUHLMAN, B. 2016. Light-induced nuclear export reveals rapid dynamics of
1218 epigenetic modifications. *Nat Chem Biol,* 12**,** 399-401.
1219 ZANCONATO, F., CORDENONSI, M. & PICCOLO, S. 2016. YAP/TAZ at the Roots of Cancer.
1220 *Cancer Cell,* 29**,** 783-803.
1221 ZANCONATO, F., CORDENONSI, M. & PICCOLO, S. 2019. YAP and TAZ: a signalling hub of
1222 the tumour microenvironment. *Nat Rev Cancer,* 19**,** 454-464.
1223 ZHAO, B., LI, L., TUMANENG, K., WANG, C. Y. & GUAN, K. L. 2010. A coordinated
1224 phosphorylation by Lats and CK1 regulates YAP stability through SCF(beta-TRCP).
1225 *Genes Dev,* 24**,** 72-85.

1226

Figure 1

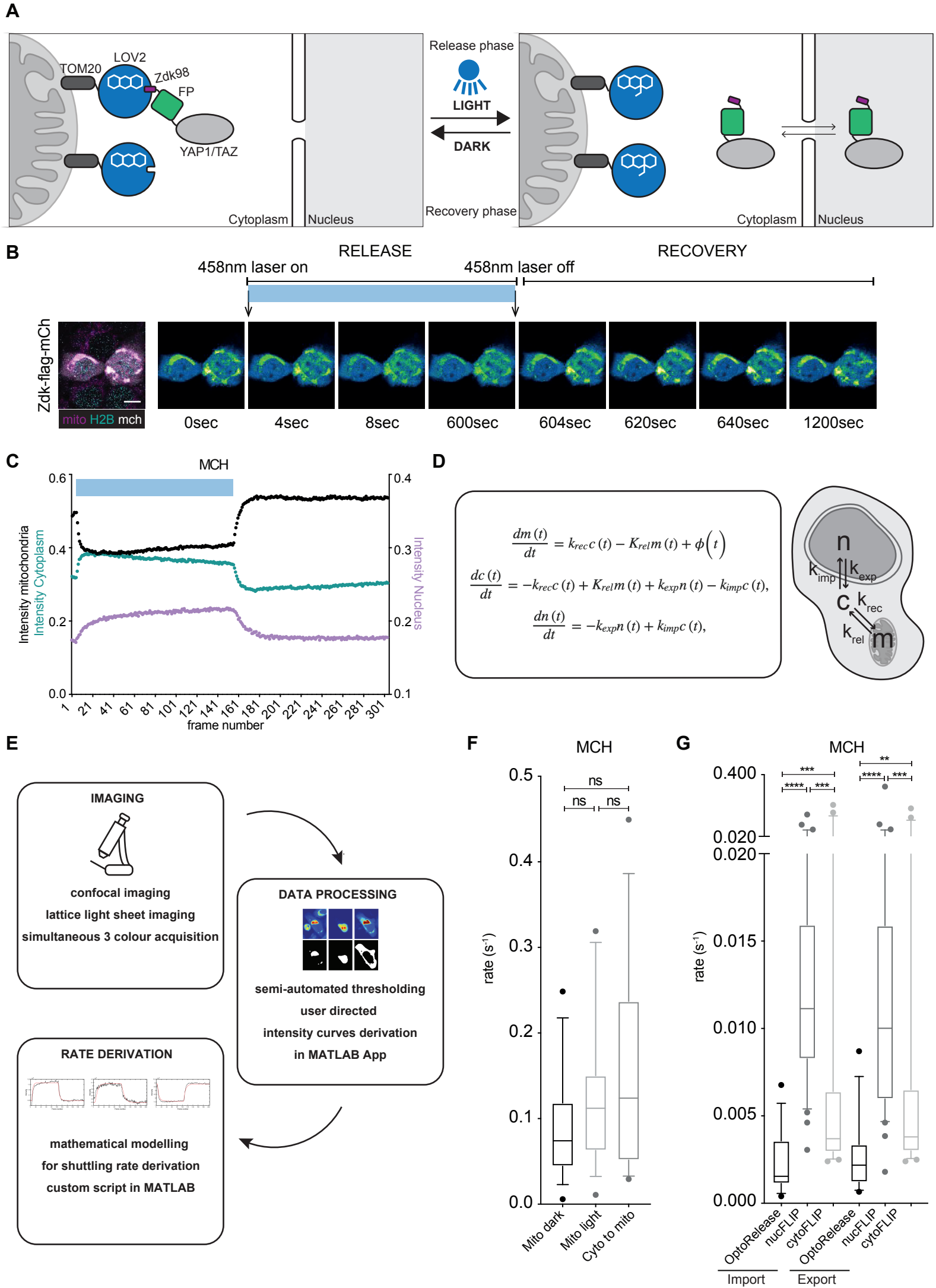
A
TOM20
LOV2
Zdk98
FP
YAP1/TAZ
Cytoplasm
Nucleus
Release phase
LIGHT
DARK
Recovery phase
Cytoplasm
Nucleus
B
RELEASE
RECOVERY
458nm laser on
458nm laser off
Zdk-flag-mCh
mito H2B mch
0sec
4sec
8sec
600sec
604sec
620sec
640sec
1200sec
C
MCH
Intensity mitochondria
Intensity Cytoplasm
Intensity Nucleus
frame number
D
$\frac{dm(t)}{dt} = k_{rec}c(t) - K_{rel}m(t) + \phi(t)$
$\frac{dc(t)}{dt} = -k_{rec}c(t) + K_{rel}m(t) + k_{exp}n(t) - k_{imp}c(t),$
$\frac{dn(t)}{dt} = -k_{exp}n(t) + k_{imp}c(t),$
n
k_{imp}
k_{exp}
c
k_{rec}
k_{rel}
m
E
IMAGING
confocal imaging
lattice light sheet imaging
simultaneous 3 colour acquisition
DATA PROCESSING
semi-automated thresholding
user directed
intensity curves derivation
in MATLAB App
RATE DERIVATION
mathematical modelling
for shuttling rate derivation
custom script in MATLAB
F
MCH
rate (s^{-1})
ns
Mito dark
Mito light
Cyto to mito
G
MCH
rate (s^{-1})
OptoRelease
nucFLIP
cytoFLIP
Import
Export

Figure 2

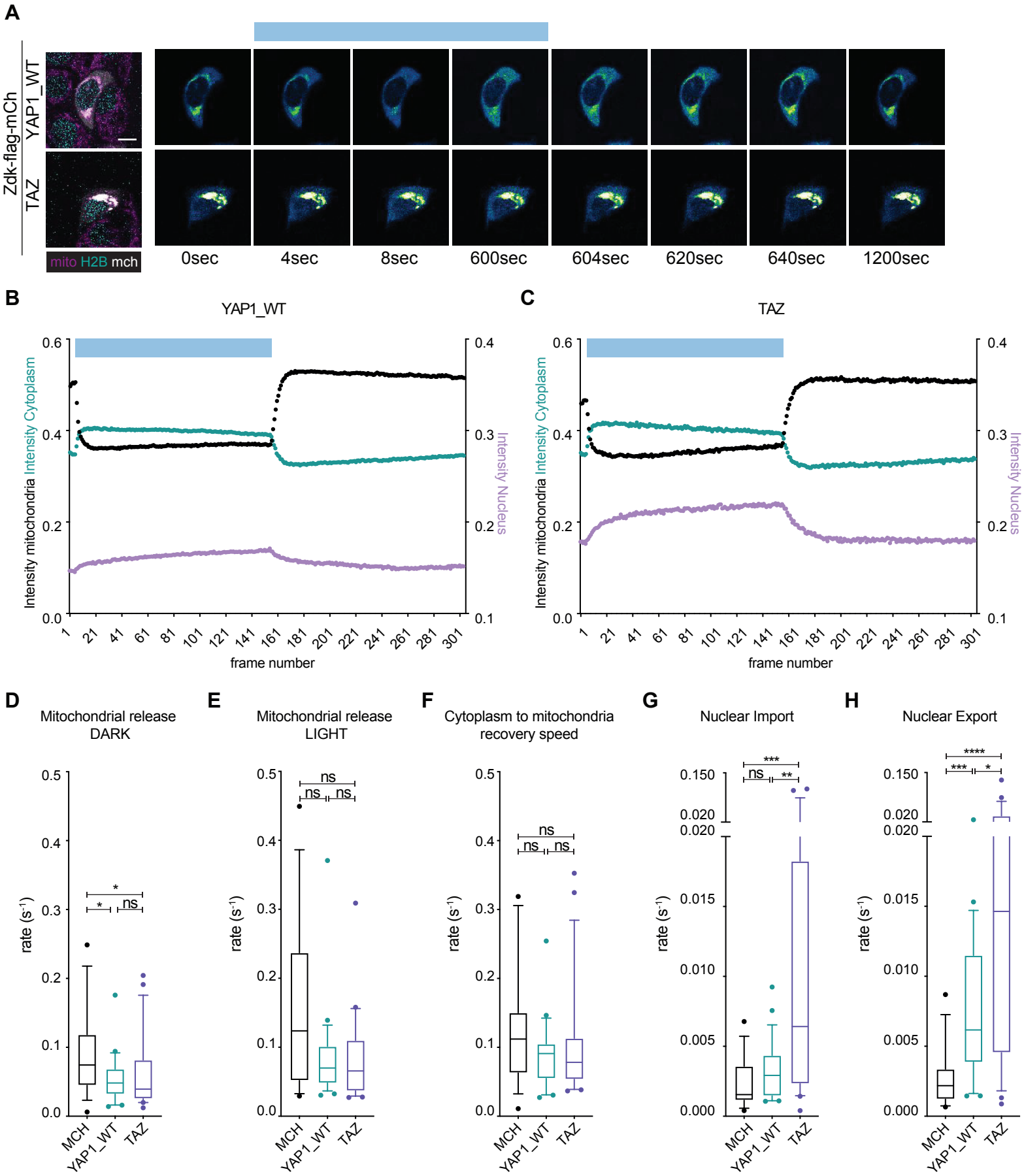
A
Zdk-flag-mCh
YAP1_WT
TAZ
mito H2B mch
0sec
4sec
8sec
600sec
604sec
620sec
640sec
1200sec
B
YAP1_WT
Intensity mitochondria Intensity Cytoplasm
Intensity Nucleus
frame number
C
TAZ
Intensity mitochondria Intensity Cytoplasm
Intensity Nucleus
frame number
D
Mitochondrial release DARK
rate (s⁻¹)
MCH
YAP1_WT
TAZ
E
Mitochondrial release LIGHT
F
Cytoplasm to mitochondria recovery speed
G
Nuclear Import
H
Nuclear Export

Figure 3

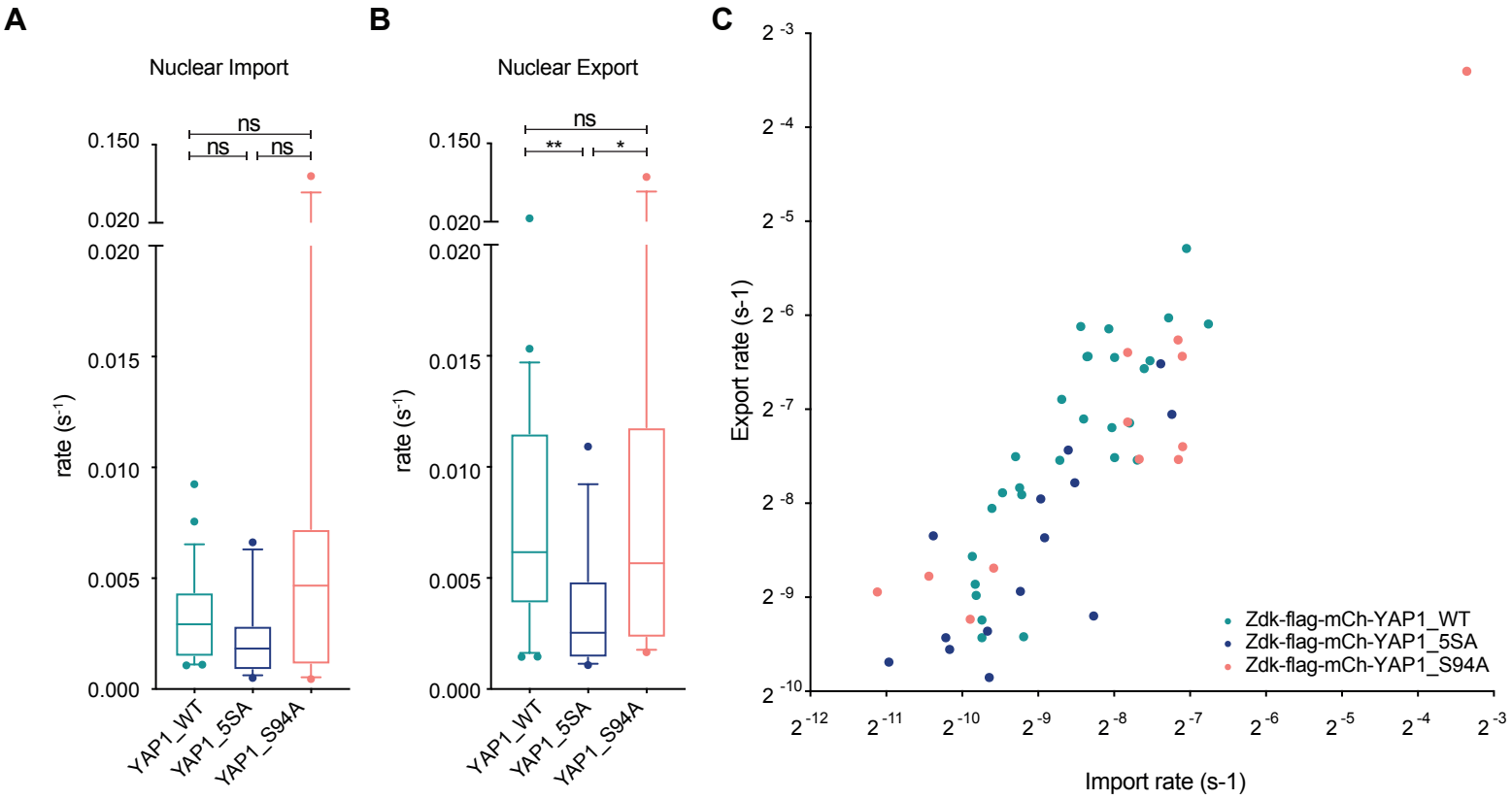
A
Nuclear Import
ns
ns
ns
0.150
0.020
0.020
0.015
0.010
0.005
0.000
rate (s-1)
YAP1_WT
YAP1_5SA
YAP1_S94A
B
Nuclear Export
ns
**
*
0.150
0.020
0.020
0.015
0.010
0.005
0.000
rate (s-1)
YAP1_WT
YAP1_5SA
YAP1_S94A
C
Export rate (s-1)
Import rate (s-1)
Zdk-flag-mCh-YAP1_WT
Zdk-flag-mCh-YAP1_5SA
Zdk-flag-mCh-YAP1_S94A

Figure 4

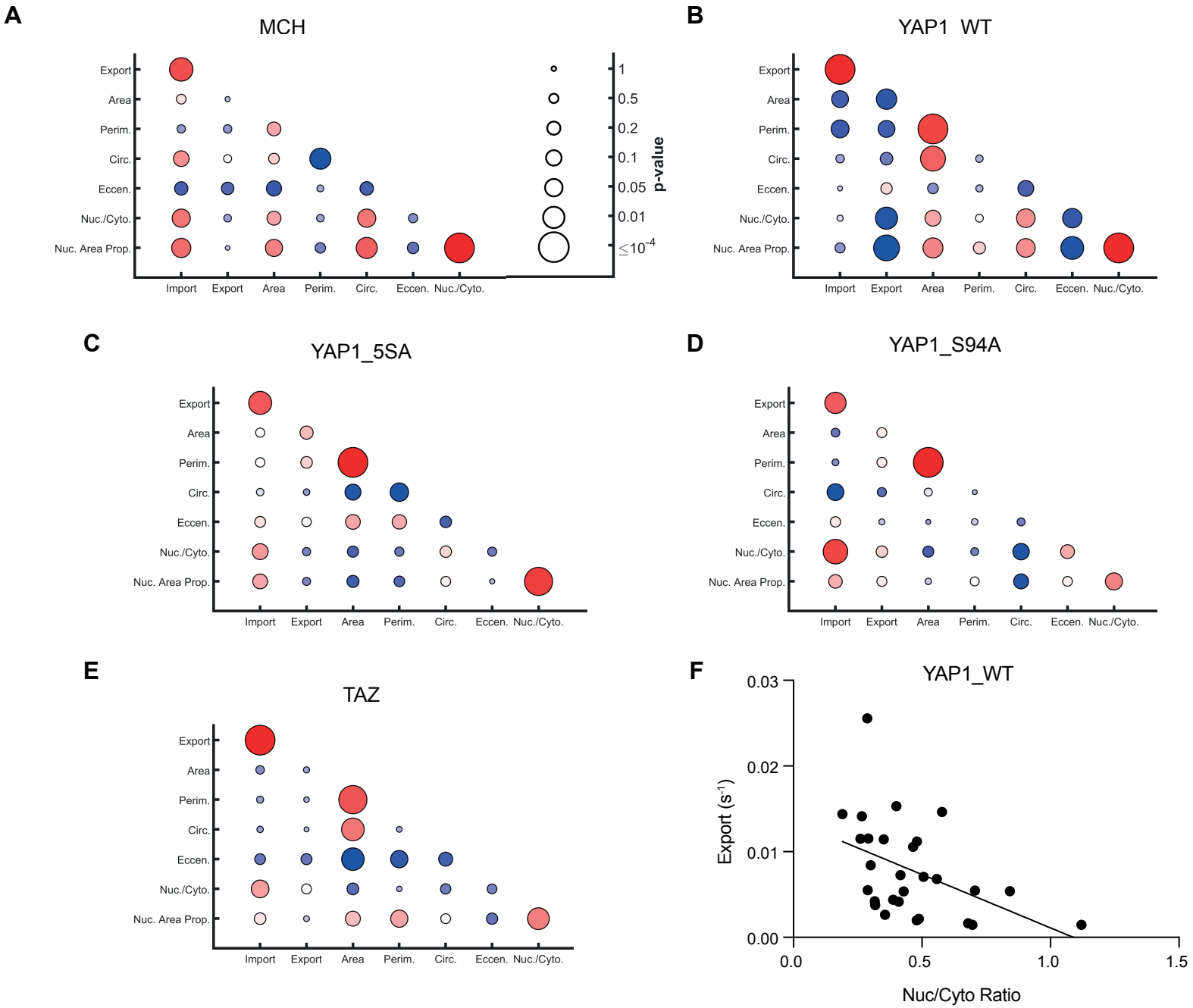
A
MCH
Export
Area
Perim.
Circ.
Eccen.
Nuc./Cyto.
Nuc. Area Prop.
Import
Export
Area
Perim.
Circ.
Eccen.
Nuc./Cyto.
1
0.5
0.2
0.1
0.05
0.01
≤10^-4
p-value
B
YAP1 WT
C
YAP1_5SA
D
YAP1_S94A
E
TAZ
F
YAP1_WT
Export (s^-1)
0.03
0.02
0.01
0.00
0.0
0.5
1.0
1.5
Nuc/Cyto Ratio

Figure 5

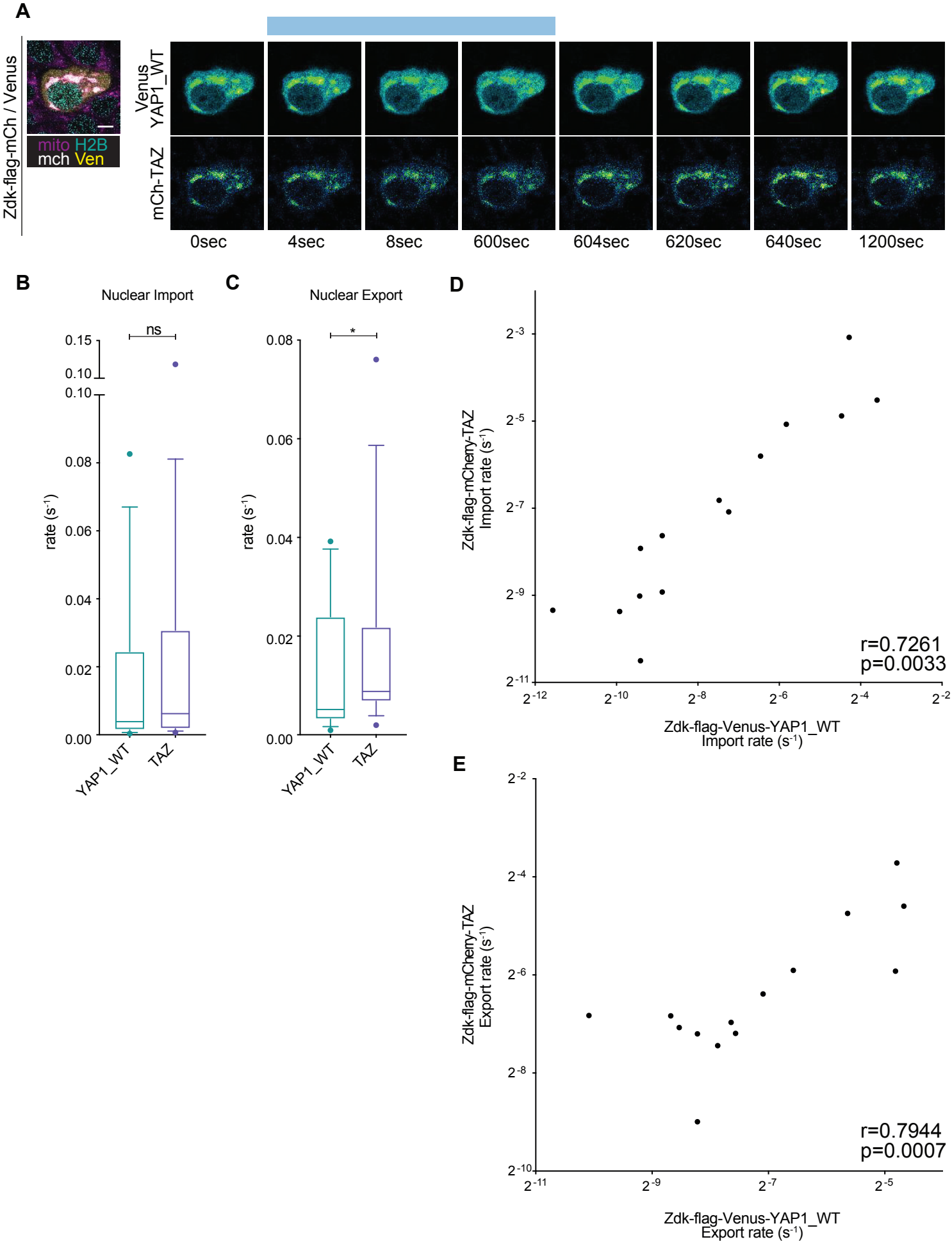
A
Zdk-flag-mCh / Venus
mito H2B
mch Ven
Venus YAP1_WT
mCh-TAZ
0sec
4sec
8sec
600sec
604sec
620sec
640sec
1200sec
B
Nuclear Import
ns
rate (s-1)
YAP1_WT
TAZ
C
Nuclear Export
*
rate (s-1)
YAP1_WT
TAZ
D
Zdk-flag-mCherry-TAZ Import rate (s-1)
Zdk-flag-Venus-YAP1_WT Import rate (s-1)
r=0.7261
p=0.0033
E
Zdk-flag-mCherry-TAZ Export rate (s-1)
Zdk-flag-Venus-YAP1_WT Export rate (s-1)
r=0.7944
p=0.0007

Figure 6

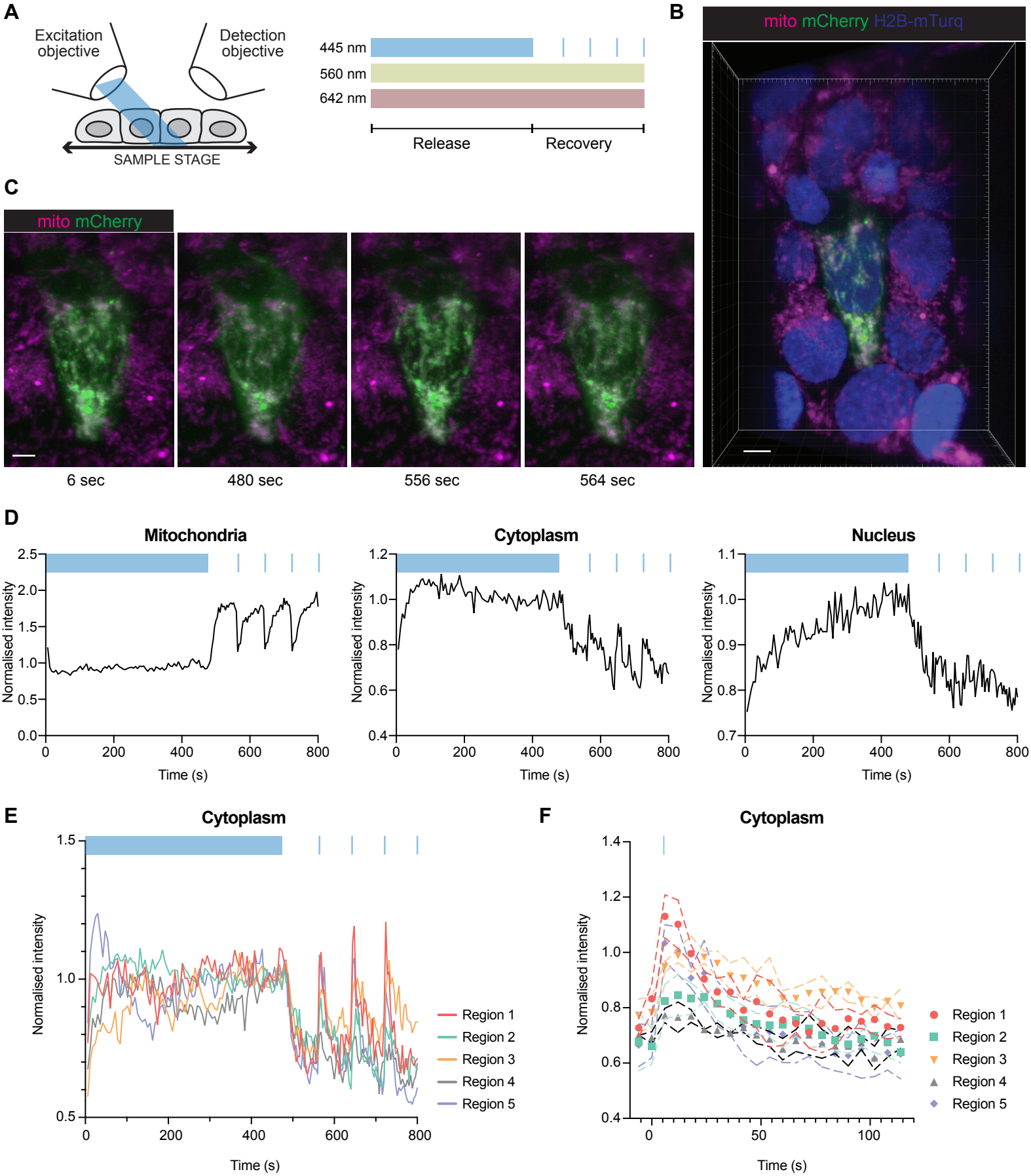
A
Excitation objective
Detection objective
SAMPLE STAGE
445 nm
560 nm
642 nm
Release
Recovery
B
mito mCherry H2B-mTurq
C
mito mCherry
6 sec
480 sec
556 sec
564 sec
D
Mitochondria
Cytoplasm
Nucleus
Normalised intensity
Time (s)
E
Cytoplasm
Region 1
Region 2
Region 3
Region 4
Region 5
F
Cytoplasm

Supplementary Figure 1

A

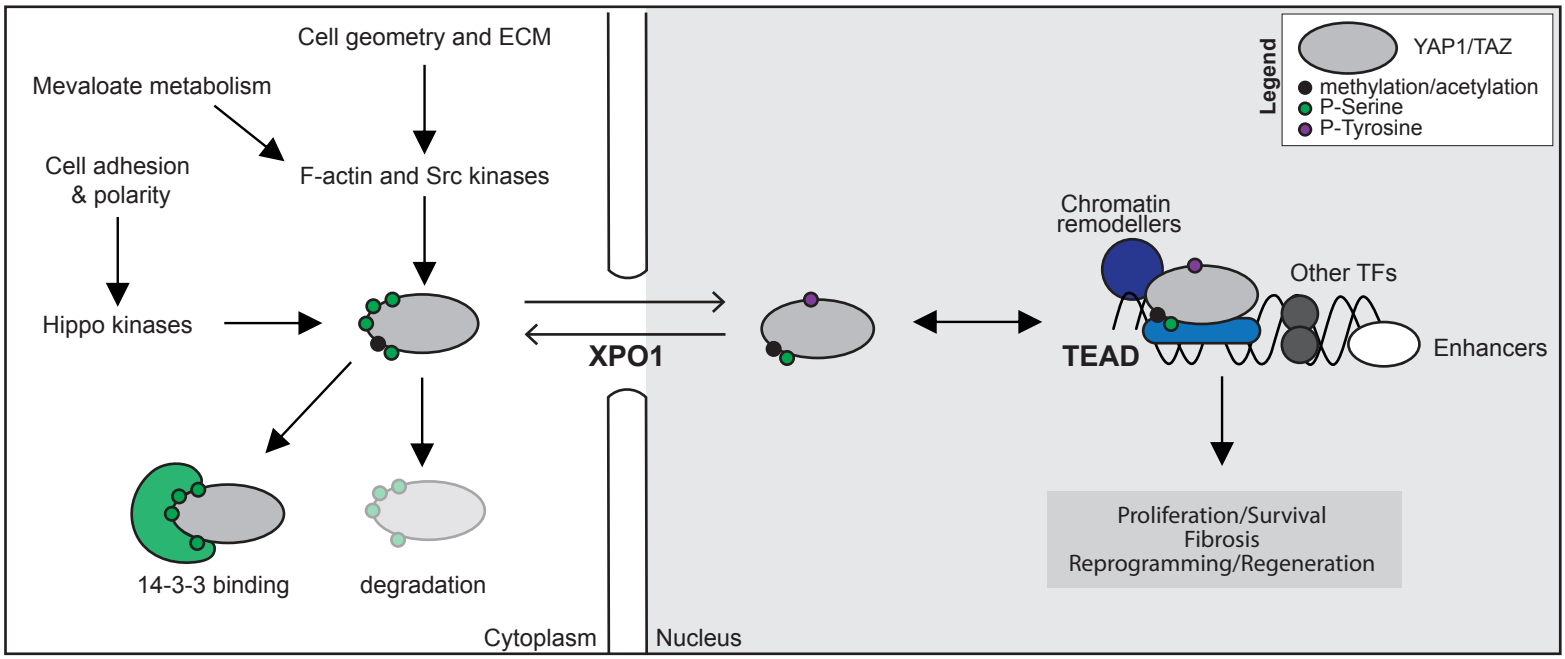

B

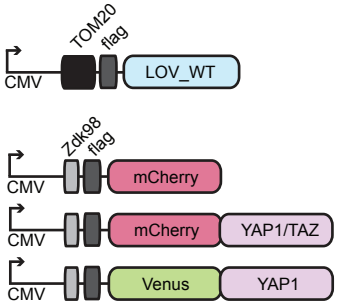

C

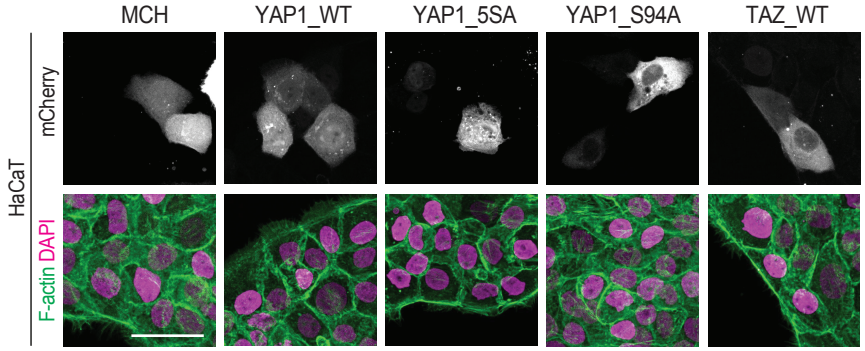

D

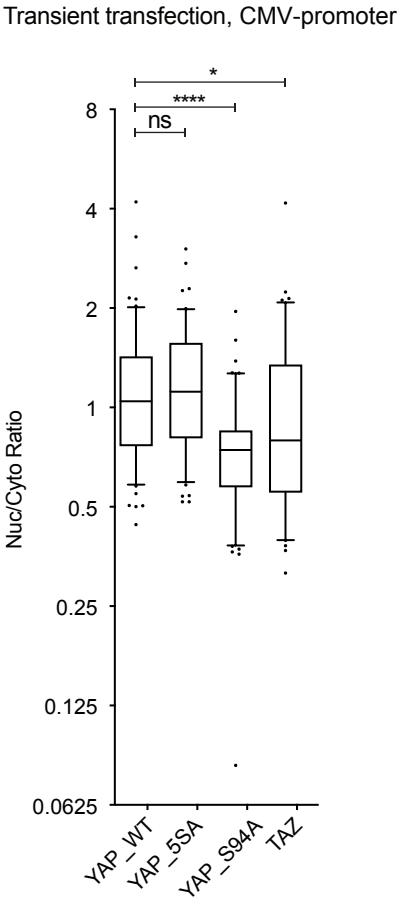

E

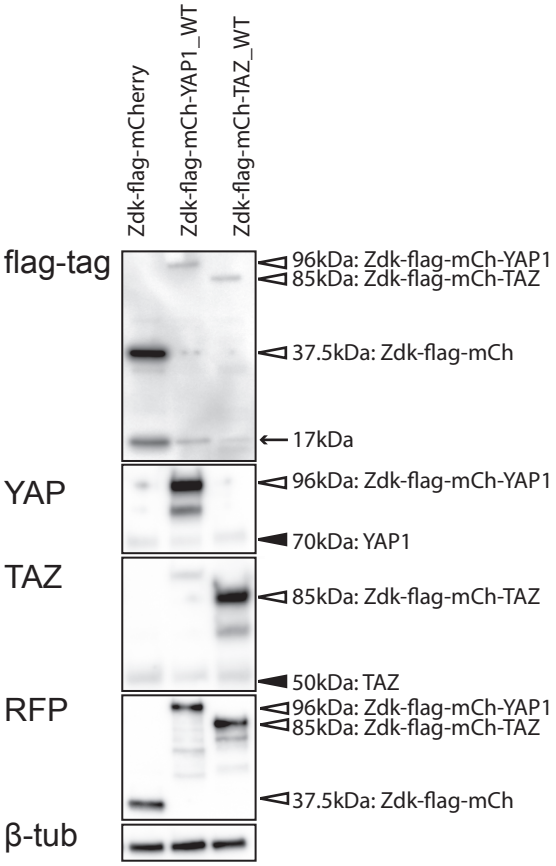

F

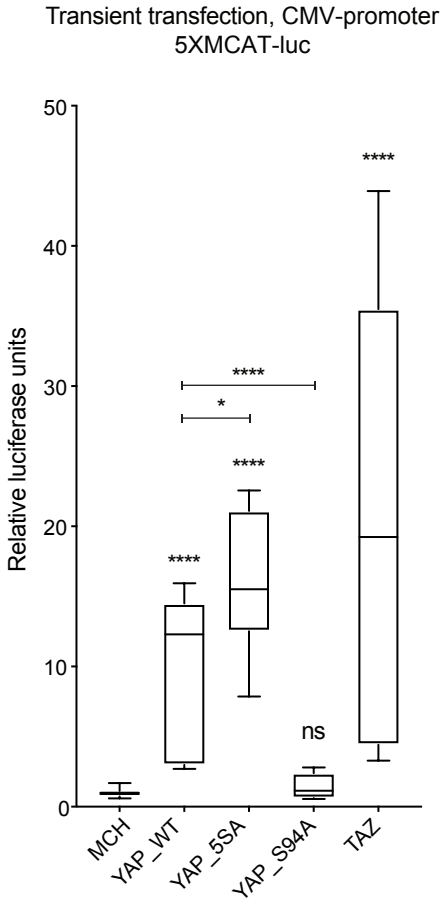

Supplementary Figure 2

A

B

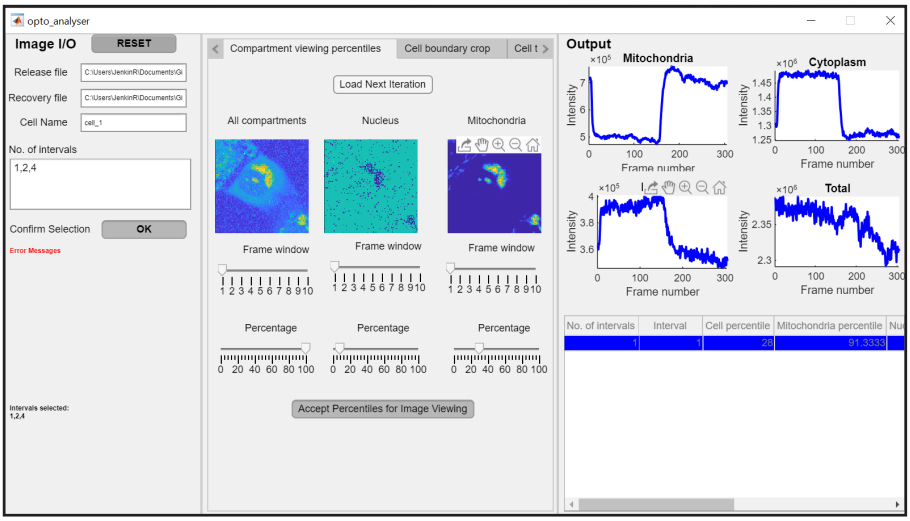

C

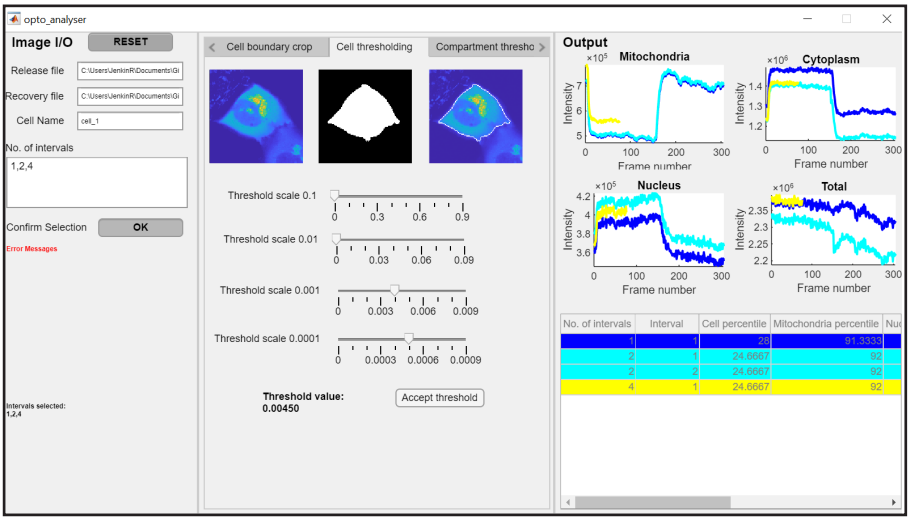

D

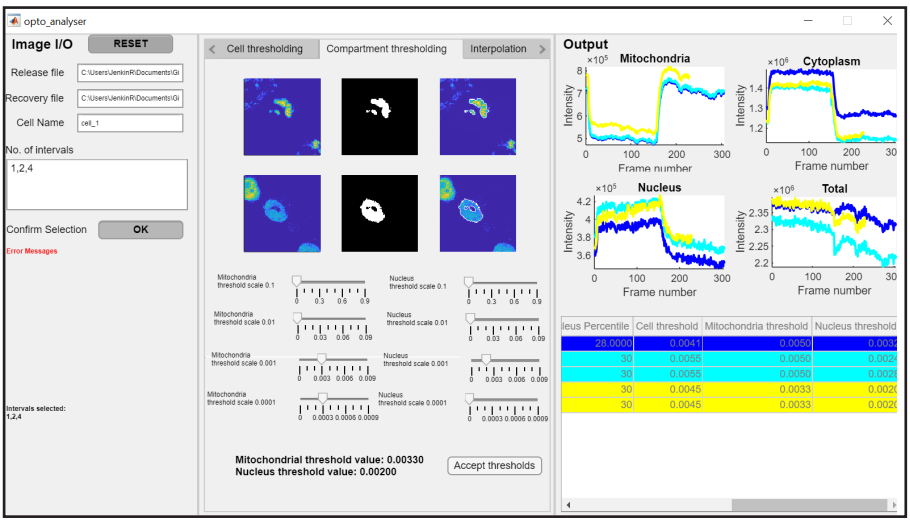

Supplementary Figure 3

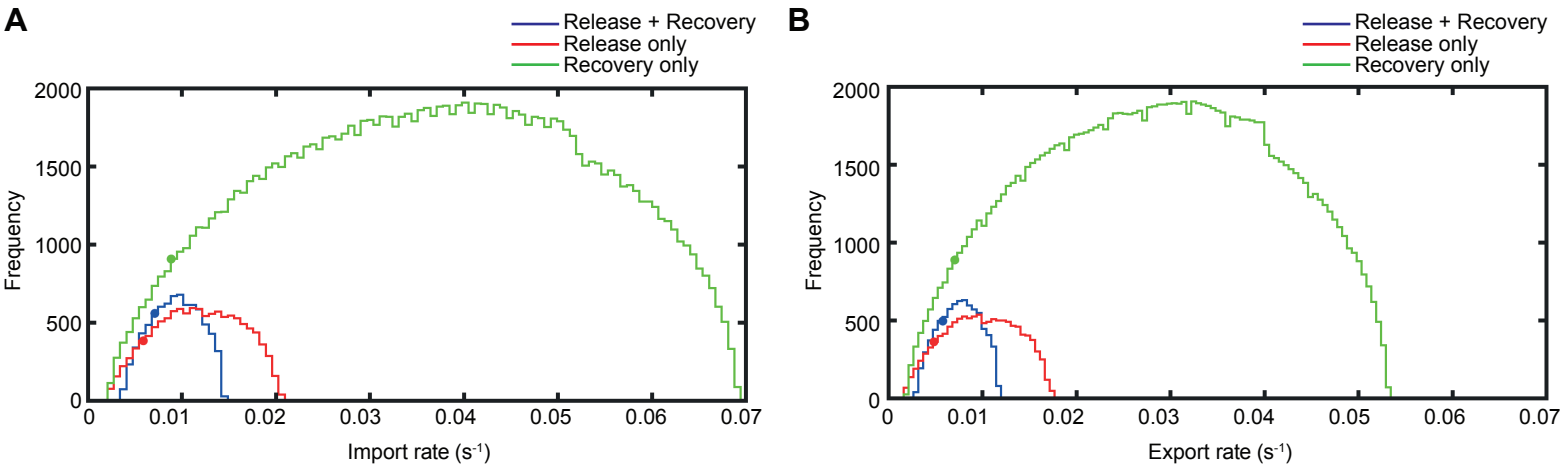

Supplementary Figure 4

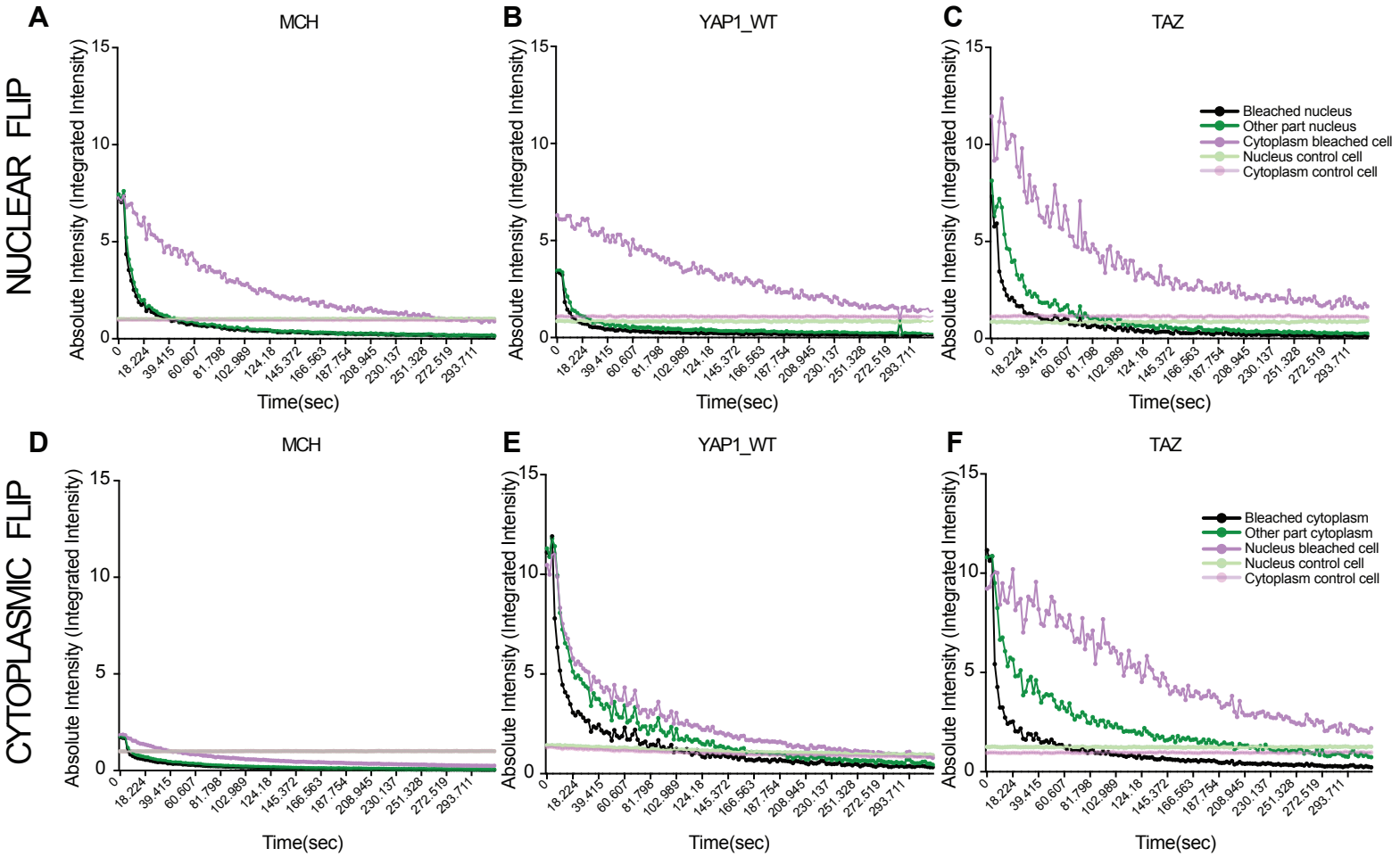

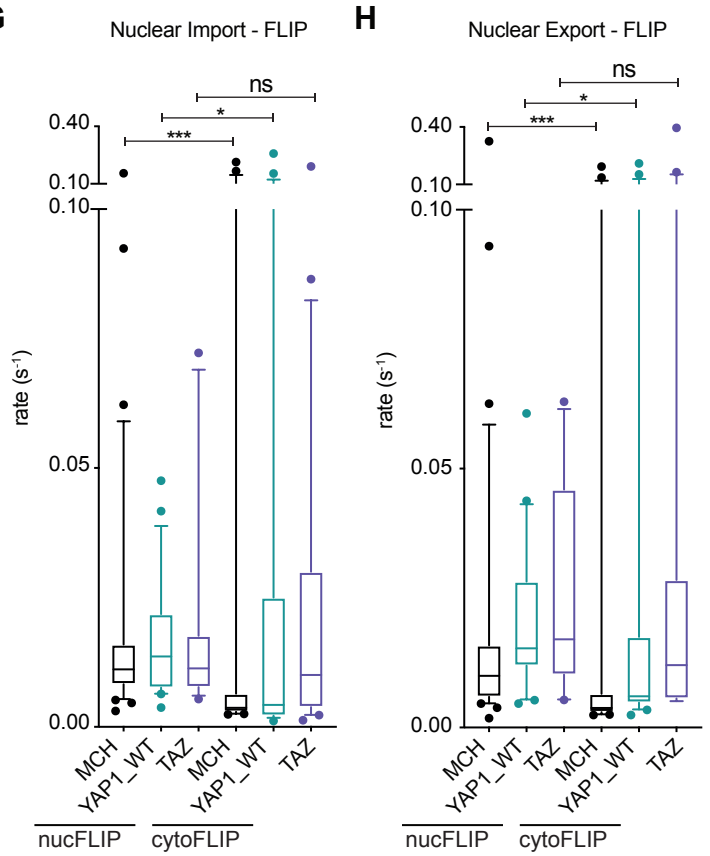

I

MEDIAN

	IMPORT (k_{in})			EXPORT (k_{out})		
construct	**Opto**	**FLIP nuc**	**FLIP cyto**	**Opto**	**FLIP nuc**	**FLIP cyto**
MCH	0.0015	0.0111	0.0037	0.0021	0.0100	0.0038
YAP1_WT	0.0029	0.0135	0.0042	0.0061	0.0153	0.0060
TAZ	0.0064	0.0113	0.0100	0.0146	0.0170	0.0120

Supplementary Figure 5

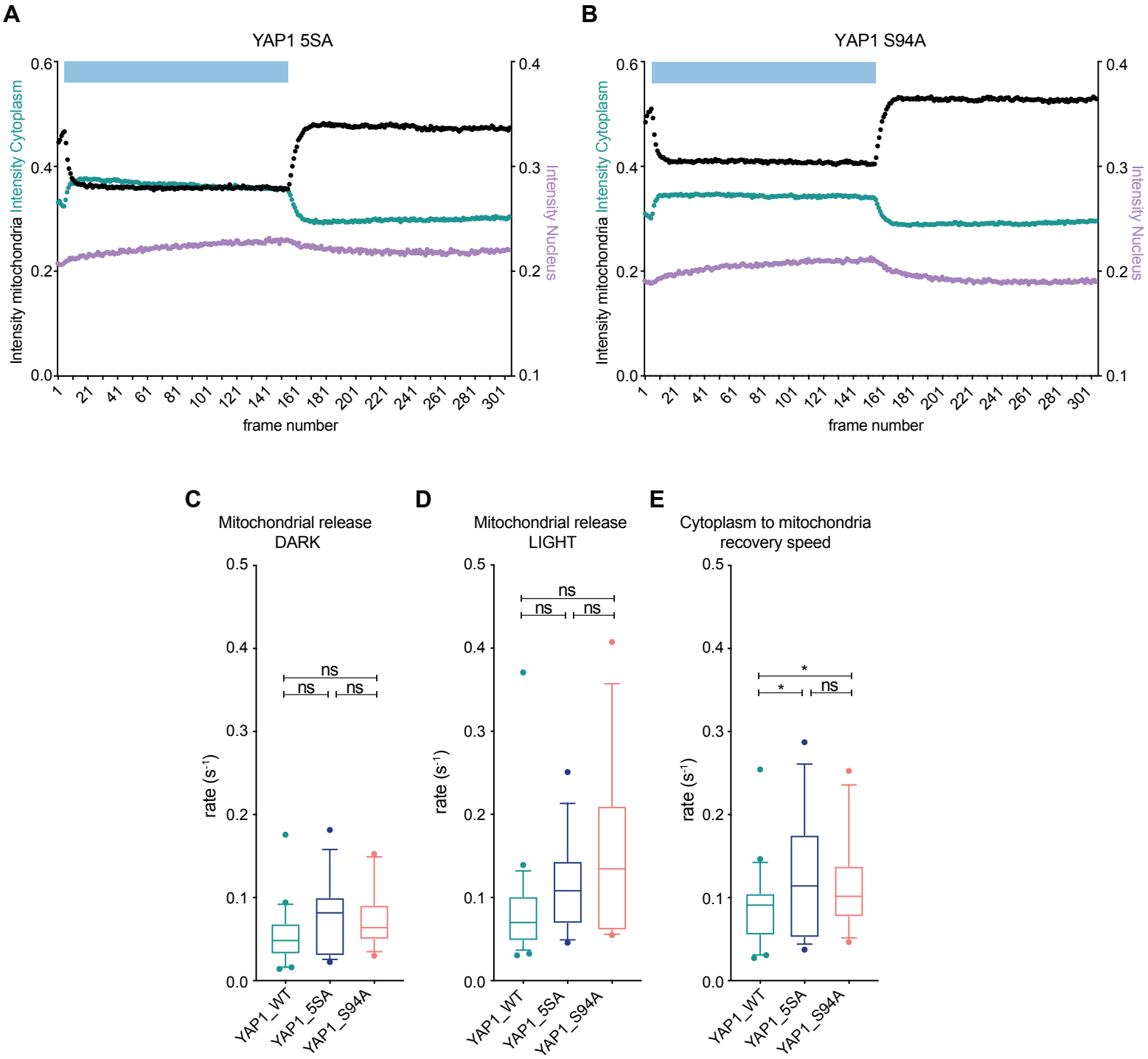

Supplementary Figure 6

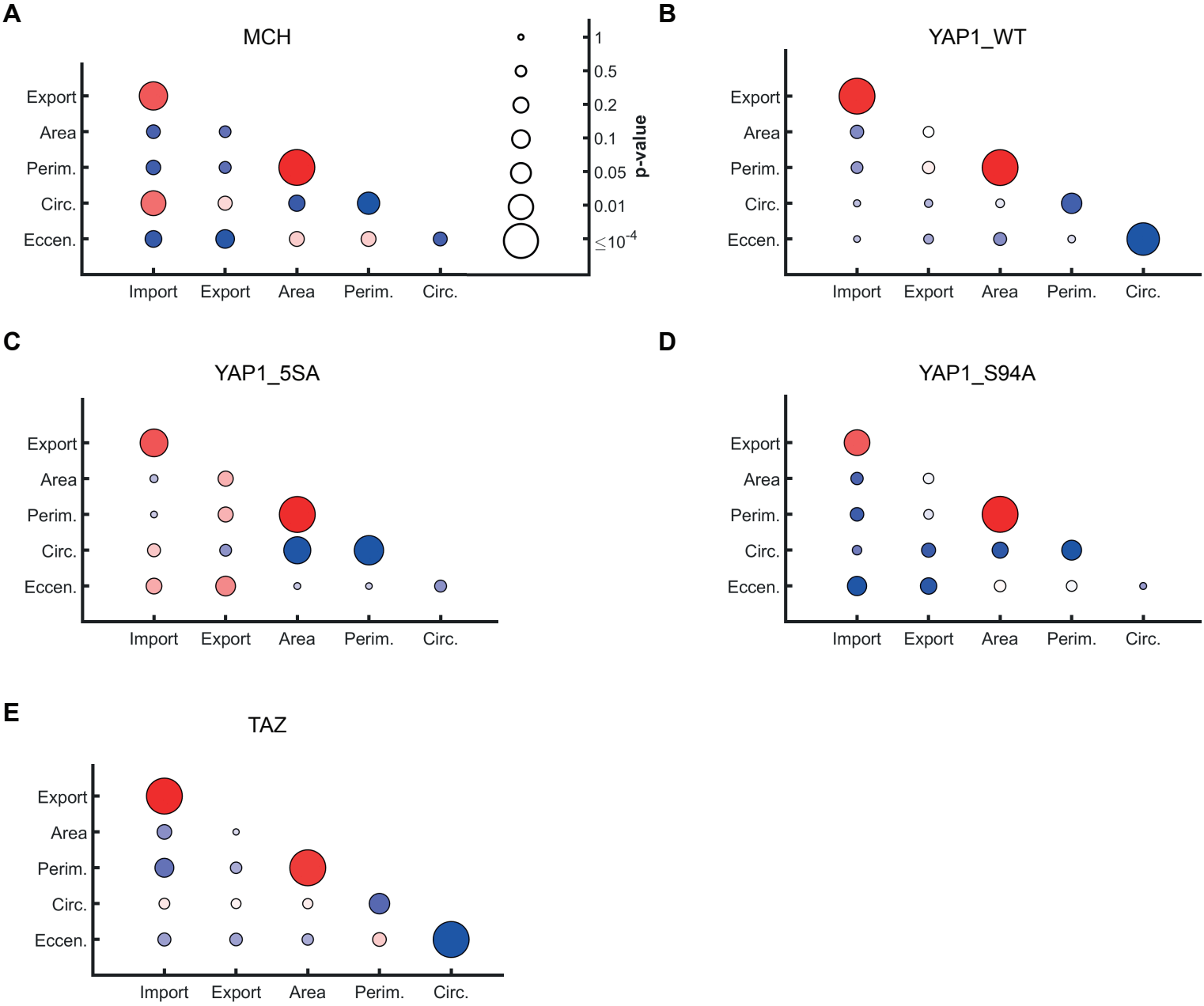

Supplementary Figure 7

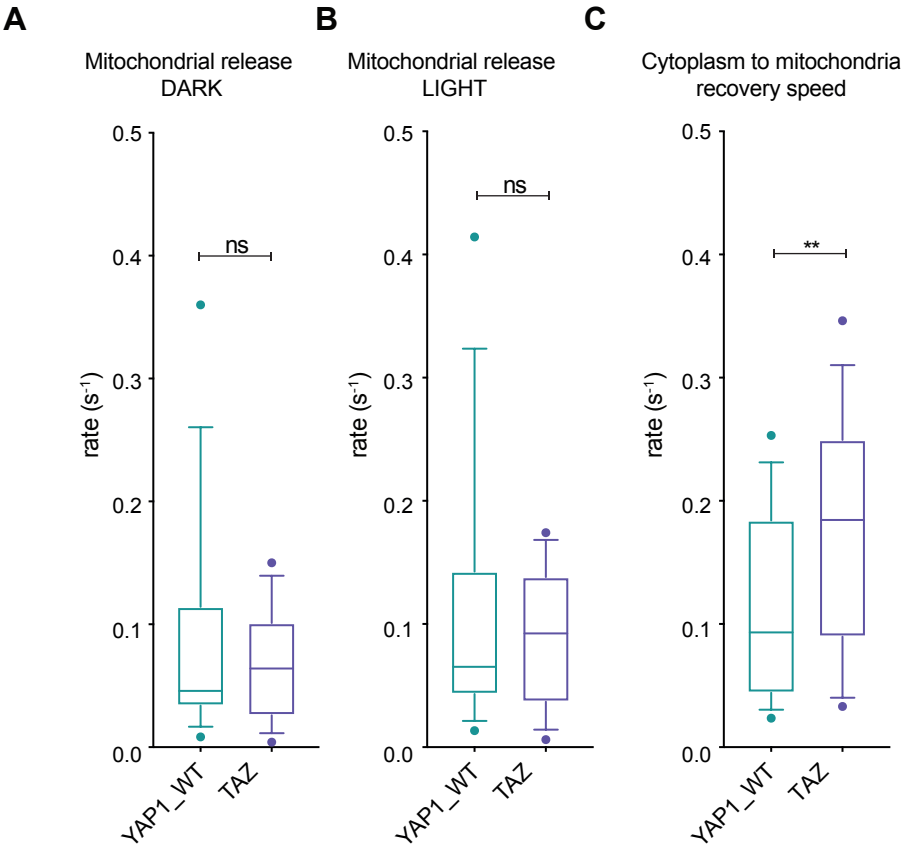
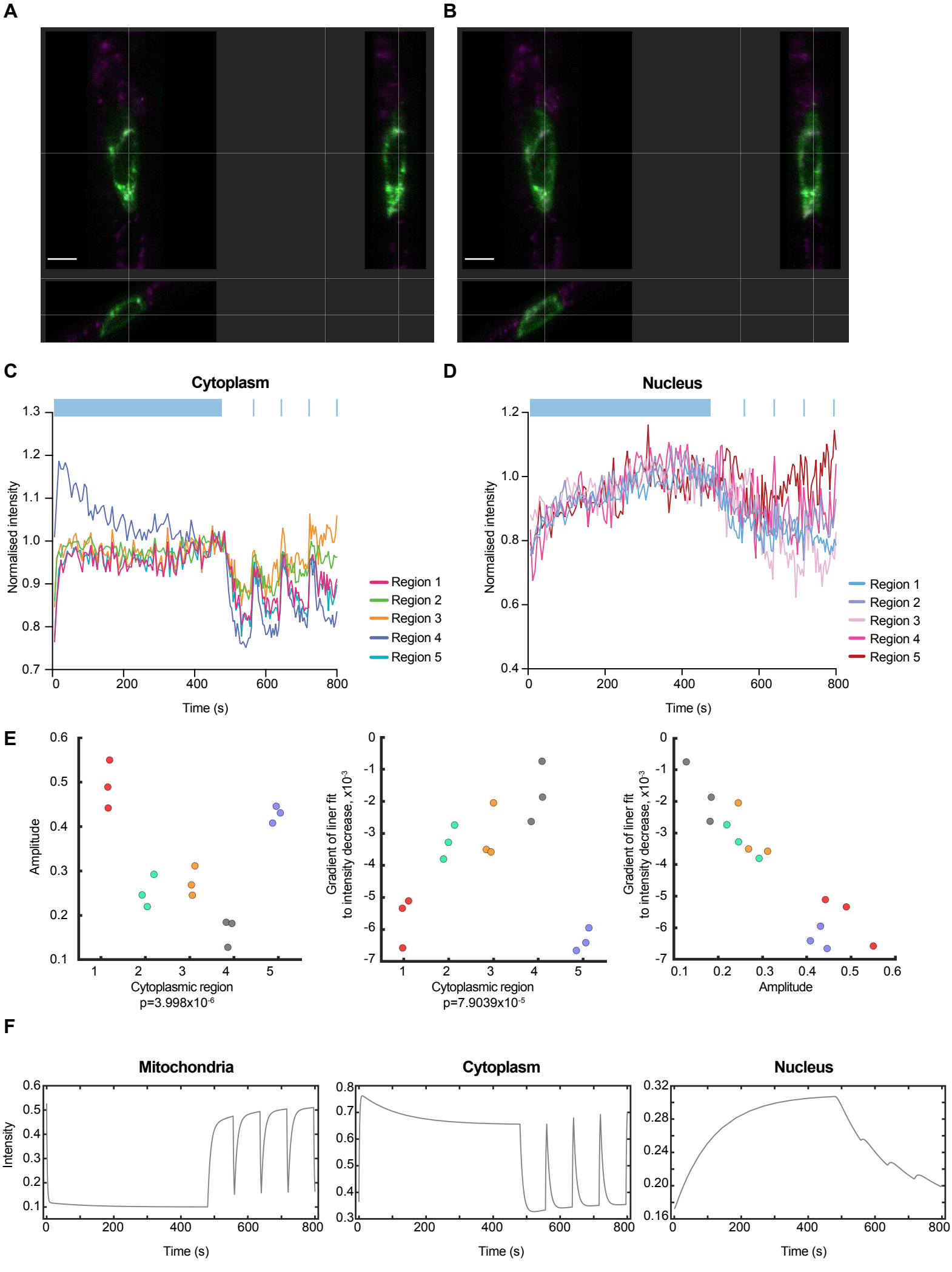
Supplementary Figure 8